

Cross-Sections and Leptonic Forward-Backward Asymmetries from the Z^0 Running of LEP

DELPHI Collaboration

Abstract

During 1993 and 1995 LEP was run at 3 energies near the Z^0 peak in order to give improved measurements of the mass and width of the resonance. During 1994, LEP operated only at the Z^0 peak. In total DELPHI accumulated data corresponding to an integrated luminosity of approximately 116 pb^{-1} . Analyses of the hadronic cross-sections and of the cross-sections and forward-backward asymmetries in the leptonic channels used the most precise evaluations of the LEP energies. In the dimuon channel, events with a photon radiated from the initial state have been used to probe the cross-sections and asymmetries down to PETRA energies. Model independent fits to all DELPHI lineshape and asymmetry data from 1990 to 1995 have been carried out giving values of the resonance parameters:

$$\begin{aligned}M_Z &= 91.1863 \pm 0.0028 \text{ GeV} \\ \Gamma_Z &= 2.4876 \pm 0.0041 \text{ GeV} \\ \sigma_0 &= 41.578 \pm 0.069 \text{ nb} \\ R_l &= 20.730 \pm 0.060 \\ A_{\text{FB}}^0 &= 0.0187 \pm 0.0019.\end{aligned}$$

These values are significantly more precise than those previously published. The results are interpreted in terms of the Standard Model.

(Accepted by E. Phys. J. C)

P. Abreu²¹, W. Adam⁵⁰, T. Adye³⁶, P. Adzic¹¹, G. D. Alekseev¹⁶, R. Alemany⁴⁹, P. P. Allport²², S. Almeded²⁴, U. Amaldi⁹, S. Amato⁴⁷, E. G. Anassontzis³, P. Andersson⁴⁴, A. Andreazza⁹, P. Antilogus²⁵, W.-D. Apel¹⁷, Y. Arnoud¹⁴, B. Åsman⁴⁴, J.-E. Augustin²⁵, A. Augustinus⁹, P. Baillon⁹, P. Bambade¹⁹, F. Barao²¹, R. Barbier²⁵, D. Y. Bardin¹⁶, G. Barker⁹, A. Baroncelli³⁸, M. Battaglia¹⁵, M. Baubillier²³, K.-H. Becks⁵², M. Begalli⁶, P. Beilliere⁸, Yu. Belokopytov^{9,53}, A. C. Benvenuti⁵, C. Berat¹⁴, M. Berggren²⁵, D. Bertini²⁵, D. Bertrand², M. Besancon³⁹, F. Bianchi⁴⁵, M. Bigi⁴⁵, M. S. Bilenky¹⁶, M.-A. Bizouard¹⁹, D. Bloch¹⁰, M. Bonesini²⁷, W. Bonivento²⁷, M. Boonekamp³⁹, P. S. L. Booth²², A. W. Borgland⁴, G. Borisov³⁹, C. Bosio⁴¹, O. Botner⁴⁸, E. Boudinov³⁰, B. Bouquet¹⁹, C. Bourdarios¹⁹, T. J. V. Bowcock²², I. Boyko¹⁶, I. Bozovic¹¹, M. Bozzo¹³, P. Branchini³⁸, T. Brenke⁵², R. A. Brenner⁴⁸, P. Bruckman³⁵, J.-M. Brunet⁸, L. Bugge³², T. Buran³², T. Burgsmueller⁵², P. Buschmann⁵², S. Cabrera⁴⁹, M. Caccia²⁷, M. Calvi²⁷, A. J. Camacho Rozas⁴⁰, T. Camporesi⁹, V. Canale³⁷, M. Canepa¹³, F. Carena⁹, L. Carroll²², C. Caso¹³, M. V. Castillo Gimenez⁴⁹, A. Cattai⁹, F. R. Cavallo⁵, Ch. Cerruti¹⁰, V. Chabaud⁹, M. Chapkin⁴², Ph. Charpentier⁹, L. Chaussard²⁵, P. Checchia³⁵, G. A. Chelkov¹⁶, M. Chen², R. Chierici⁴⁵, P. Chliapnikov⁴², P. Chochula⁷, V. Chorowicz²⁵, J. Chudoba²⁹, P. Collins⁹, M. Colomer⁴⁹, R. Contri¹³, E. Cortina⁴⁹, G. Cosme¹⁹, F. Cossutti³⁹, J.-H. Cowell²², H. B. Crawley¹, D. Crennell³⁶, G. Crosetti¹³, J. Cuevas Maestro³³, S. Czellar¹⁵, B. Dalmagne¹⁹, G. Damgaard²⁸, M. Davenport⁹, W. Da Silva²³, A. Deghorain², G. Della Ricca⁴⁶, P. Delpierre²⁶, N. Demaria⁹, A. De Angelis⁹, W. De Boer¹⁷, S. De Brabandere², C. De Clercq², B. De Lotto⁴⁶, A. De Min³⁵, L. De Paula⁴⁷, H. Dijkstra⁹, L. Di Ciaccio³⁷, A. Di Diodato³⁷, A. Djannati⁸, J. Dolbeau⁸, K. Doroba⁵¹, M. Dracos¹⁰, J. Drees⁵², K.-A. Drees⁵², M. Dris³¹, A. Duperrin²⁵, J.-D. Durand^{25,9}, R. Ehret¹⁷, G. Eigen⁴, T. Ekelof⁴⁸, G. Ekspong⁴⁴, M. Ellert⁴⁸, M. Elsing⁹, J.-P. Engel¹⁰, B. Erzen⁴³, M. Espirito Santo²¹, E. Falk²⁴, G. Fanourakis¹¹, D. Fassouliotis¹¹, J. Fayot²³, M. Feindt¹⁷, A. Fenyuk⁴², P. Ferrari²⁷, A. Ferrer⁴⁹, S. Fichet²³, A. Firestone¹, P.-A. Fischer⁹, U. Flagmeyer⁵², H. Foeth⁹, E. Fokitis³¹, F. Fontanelli¹³, B. Franek³⁶, A. G. Frodesen⁴, R. Fruhwirth⁵⁰, F. Fulda-Quenzer¹⁹, J. Fuster⁴⁹, A. Galloni²², D. Gamba⁴⁵, M. Gandelman⁴⁷, C. Garcia⁴⁹, J. Garcia⁴⁰, C. Gaspar⁹, M. Gaspar⁴⁷, U. Gasparini³⁵, Ph. Gaviillet⁹, E. N. Gaziz³¹, D. Gele¹⁰, J.-P. Gerber¹⁰, L. Gerdyukov⁴², N. Ghodbane²⁵, I. Gil⁴⁹, F. Glege⁵², R. Gokieli⁵¹, B. Golob⁴³, P. Goncalves²¹, I. Gonzalez Caballero⁴⁰, G. Gopal³⁶, L. Gorn^{1,54}, M. Gorski⁵¹, Yu. Gouz⁴², V. Gracco¹³, J. Grahl¹, E. Graziani³⁸, C. Green²², A. Grefrath⁵², P. Gris³⁹, K. Grzelak⁵¹, M. Gunther⁴⁸, J. Guy³⁶, F. Hahn⁹, S. Hahn⁵², S. Haider⁹, A. Hallgren⁴⁸, K. Hamacher⁵², F. J. Harris³⁴, V. Hedberg²⁴, S. Heising¹⁷, R. Henriques²¹, J. J. Hernandez⁴⁹, P. Herquet², H. Herr⁹, T. L. Hessing³⁴, J.-M. Heuser⁵², E. Higon⁴⁹, S.-O. Holmgren⁴⁴, P. J. Holt³⁴, D. Holthuizen³⁰, S. Hoorelbeke², M. Houlden²², J. Hrubec⁵⁰, K. Huet², K. Hultqvist⁴⁴, J. N. Jackson²², R. Jacobsson⁴⁴, P. Jalocho⁹, R. Janik⁷, Ch. Jarlskog²⁴, G. Jarlskog²⁴, P. Jarry³⁹, B. Jean-Marie¹⁹, E. K. Johansson⁴⁴, P. Jonsson²⁴, C. Joram⁹, P. Juillot¹⁰, F. Kapusta²³, K. Karafasoulis¹¹, S. Katsanevas²⁵, E. C. Katsoufis³¹, R. Keranen¹⁷, B. A. Khomenko¹⁶, N. N. Khovanski¹⁶, A. Kiiskinen¹⁵, B. King²², N. J. Kjaer³⁰, O. Klapp⁵², H. Klein⁹, P. Kluit³⁰, D. Knoblauch¹⁷, P. Kokkinias¹¹, A. Konopliannikov⁴², M. Koratzinos⁹, V. Kostioukhine⁴², C. Kourkoumelis³, O. Kouznetsov¹⁶, M. Kramer⁵⁰, C. Kreuter⁹, E. Kriznic⁴³, J. Krstic¹¹, Z. Krumstein¹⁶, P. Kubinec⁷, W. Kucewicz¹⁸, K. Kurvinen¹⁵, J. W. Lamsa¹, L. Lanceri⁴⁶, D. W. Lane¹, P. Langefeld⁵², V. Lapin⁴², J.-P. Laugier³⁹, R. Lauhakangas¹⁵, G. Leder⁵⁰, F. Ledroit¹⁴, V. Lefebure², L. Leinonen⁴⁴, A. Leisos¹¹, R. Leitner²⁹, J. Lemonne², G. Lenzen⁵², V. Lepeltier¹⁹, T. Lesiak¹⁸, M. Lethuillier³⁹, J. Libby³⁴, D. Liko⁹, A. Lipniacka⁴⁴, I. Lippi³⁵, B. Loerstad²⁴, M. Lokajicek¹², J. G. Loken³⁴, J. H. Lopes⁴⁷, J. M. Lopez⁴⁰, R. Lopez-Fernandez¹⁴, D. Loukas¹¹, P. Lutz³⁹, L. Lyons³⁴, J. MacNaughton⁵⁰, J. R. Mahon⁶, A. Maio²¹, A. Malek⁵², T. G. M. Malmgren⁴⁴, V. Malychhev¹⁶, F. Mandl⁵⁰, J. Marco⁴⁰, R. Marco⁴⁰, B. Marechal⁴⁷, M. Margoni³⁵, J.-C. Marin⁹, C. Mariotti⁹, A. Markou¹¹, C. Martinez-Rivero³³, F. Martinez-Vidal⁴⁹, S. Marti i Garcia²², N. Mastroiannopoulos¹¹, F. Matorras⁴⁰, C. Matteuzzi²⁷, G. Matthiae³⁷, J. Mazik²⁹, F. Mazzucato³⁵, M. Mazzucato³⁵, M. Mc Cubbin²², R. Mc Kay¹, R. Mc Nulty⁹, G. Mc Pherson²², C. Meroni²⁷, E. Migliore⁴⁵, L. Mirabito²⁵, W. A. Mitaroff⁵⁰, U. Mjoernmark²⁴, T. Moa⁴⁴, R. Moeller²⁸, K. Moenig⁹, M. R. Monge¹³, X. Moreau²³, P. Morettini¹³, G. Morton³⁴, K. Muenich⁵², M. Mulders³⁰, C. Mulet-Marquis¹⁴, R. Muresan²⁴, W. J. Murray³⁶, B. Muryn^{14,18}, G. Myatt³⁴, T. Myklebust³², F. Naraghi¹⁴, F. L. Navarria⁵, S. Navas⁴⁹, K. Nawrocki⁵¹, P. Negri²⁷, N. Neufeld⁹, W. Neumann⁵², N. Neumeister⁵⁰, R. Nicolaidou¹⁴, B. S. Nielsen²⁸, M. Nieuwenhuizen³⁰, V. Nikolaenko¹⁰, M. Nikolenko^{10,16}, V. Nomokonov¹⁵, A. Normand²², A. Nygren²⁴, V. Obraztsov⁴², A. G. Olshevski¹⁶, A. Onofre²¹, R. Orava¹⁵, G. Orazi¹⁰, K. Osterberg¹⁵, A. Ouraou³⁹, P. Paganini¹⁹, M. Paganoni²⁷, S. Paiano⁵, R. Pain²³, R. Paiva²¹, J. Palacios³⁴, H. Palka¹⁸, Th. D. Papadopoulou³¹, K. Papageorgiou¹¹, L. Pape⁹, C. Parkes³⁴, F. Parodi¹³, U. Parzefall²², A. Passeri³⁸, M. Pegoraro³⁵, L. Peralta²¹, M. Pernicka⁵⁰, A. Perrotta⁵, C. Petridou⁴⁶, A. Petrolini¹³, H. T. Phillips³⁶, G. Piana¹³, F. Pierre³⁹, M. Pimenta²¹, E. Pionto²⁷, T. Podobnik⁴³, M. E. Pol⁶, G. Polok¹⁸, P. Poropat⁴⁶, V. Pozdniakov¹⁶, P. Privitera³⁷, N. Pukhaeva¹⁶, A. Pullia²⁷, D. Radojicic³⁴, S. Ragazzi²⁷, H. Rahmani³¹, D. Rakoczy⁵⁰, P. N. Ratoff²⁰, A. L. Read³², P. Rebecchi⁹, N. G. Redaelli²⁷, M. Regler⁵⁰, D. Reid⁹, R. Reinhardt⁵², P. B. Renton³⁴, L. K. Resvanis³, F. Richard¹⁹, J. Ridky¹², G. Rinaudo⁴⁵, O. Rohne³², A. Romero⁴⁵, P. Ronchese³⁵, E. I. Rosenberg¹, P. Rosinsky⁷, P. Roudeau¹⁹, T. Rovelli⁵, V. Ruhlmann-Kleider³⁹, A. Ruiz⁴⁰, H. Saarikko¹⁵, Y. Sacquin³⁹, A. Sadovsky¹⁶, G. Sajot¹⁴, J. Salt⁴⁹, D. Sampsonidis¹¹, M. Sannino¹³, H. Schneider¹⁷, Ph. Schwemling²³, U. Schwickerath¹⁷, M. A. E. Schyns⁵², F. Scuri⁴⁶, P. Seager²⁰, Y. Sedykh¹⁶, A. M. Segar³⁴, R. Sekulin³⁶, R. C. Shellard⁶, A. Sheridan²², R. Silvestre³⁹, L. Simard³⁹, F. Simonetto³⁵, A. N. Sisakian¹⁶, T. B. Skaali³², G. Smadja²⁵, O. Smirnova²⁴, G. R. Smith³⁶, A. Sopczak¹⁷, R. Sosnowski⁵¹, T. Spassov²¹, E. Spiriti³⁸, P. Sponholz⁵², S. Squarcia¹³, D. Stampfer⁵⁰, C. Stanescu³⁸, S. Stanic⁴³, S. Stapnes³², K. Stevenson³⁴, A. Stocchi¹⁹, J. Strauss⁵⁰, R. Strub¹⁰, B. Stugu⁴, M. Szczekowski⁵¹, M. Szeptycka⁵¹, T. Tabarelli²⁷, F. Tegenfeldt⁴⁸, F. Terranova²⁷, J. Thomas³⁴, A. Tilquin²⁶, J. Timmermans³⁰, L. G. Tkatchev¹⁶, T. Todorov¹⁰, S. Todorova¹⁰

D.Z.Toet³⁰, A.Tomaradze², A.Tonazzo²⁷, L.Tortora³⁸, G.Transtromer²⁴, D.Treille⁹, G.Tristram⁸, A.Trombini¹⁹, C.Troncon²⁷, A.Tsirou⁹, M-L.Turluer³⁹, I.A.Tyapkin¹⁶, S.Tzamaras¹¹, B.Ueberschaer⁵², O.Ullaland⁹, V.Uvarov⁴², G.Valenti⁵, E.Vallazza⁴⁶, C.Vander Velde², G.W.Van Apeldoorn³⁰, P.Van Dam³⁰, W.K.Van Doninck², J.Van Eldik³⁰, A.Van Lysebetten², I.Van Vulpen³⁰, N.Vassilopoulos³⁴, G.Vegni²⁷, L.Ventura³⁵, W.Venus³⁶, F.Verbeure², M.Verlato³⁵, L.S.Vertogradov¹⁶, V.Verzi³⁷, D.Vilanova³⁹, L.Vitale⁴⁶, E.Vlasov⁴², A.S.Vodopyanov¹⁶, G.Voulgaris³, V.Vrba¹², H.Wahlen⁵², C.Walck⁴⁴, C.Weiser¹⁷, A.M.Wetherell⁹, D.Wicke⁵², J.H.Wickens², G.R.Wilkinson⁹, M.Winter¹⁰, M.Witek¹⁸, T.Wlodek¹⁹, G.Wolf⁹, J.Yi¹, O.Yushchenko⁴², A.Zaitsev⁴², A.Zalewska¹⁸, P.Zalewski⁵¹, D.Zavrtanik⁴³, E.Zevgolatakos¹¹, N.I.Zimin^{16,24}, G.C.Zucchelli⁴⁴, G.Zumerle³⁵

¹Department of Physics and Astronomy, Iowa State University, Ames IA 50011-3160, USA

²Physics Department, Univ. Instelling Antwerpen, Universiteitsplein 1, BE-2610 Wilrijk, Belgium and IIHE, ULB-VUB, Pleinlaan 2, BE-1050 Brussels, Belgium

and Faculté des Sciences, Univ. de l'Etat Mons, Av. Maistriau 19, BE-7000 Mons, Belgium

³Physics Laboratory, University of Athens, Solonos Str. 104, GR-10680 Athens, Greece

⁴Department of Physics, University of Bergen, Allégaten 55, NO-5007 Bergen, Norway

⁵Dipartimento di Fisica, Università di Bologna and INFN, Via Irnerio 46, IT-40126 Bologna, Italy

⁶Centro Brasileiro de Pesquisas Físicas, rua Xavier Sigaud 150, BR-22290 Rio de Janeiro, Brazil

and Depto. de Física, Pont. Univ. Católica, C.P. 38071 BR-22453 Rio de Janeiro, Brazil

and Inst. de Física, Univ. Estadual do Rio de Janeiro, rua São Francisco Xavier 524, Rio de Janeiro, Brazil

⁷Comenius University, Faculty of Mathematics and Physics, Mlynska Dolina, SK-84215 Bratislava, Slovakia

⁸Collège de France, Lab. de Physique Corpusculaire, IN2P3-CNRS, FR-75231 Paris Cedex 05, France

⁹CERN, CH-1211 Geneva 23, Switzerland

¹⁰Institut de Recherches Subatomiques, IN2P3 - CNRS/ULP - BP20, FR-67037 Strasbourg Cedex, France

¹¹Institute of Nuclear Physics, N.C.S.R. Demokritos, P.O. Box 60228, GR-15310 Athens, Greece

¹²FZU, Inst. of Phys. of the C.A.S. High Energy Physics Division, Na Slovance 2, CZ-180 40, Praha 8, Czech Republic

¹³Dipartimento di Fisica, Università di Genova and INFN, Via Dodecaneso 33, IT-16146 Genova, Italy

¹⁴Institut des Sciences Nucléaires, IN2P3-CNRS, Université de Grenoble 1, FR-38026 Grenoble Cedex, France

¹⁵Helsinki Institute of Physics, HIP, P.O. Box 9, FI-00014 Helsinki, Finland

¹⁶Joint Institute for Nuclear Research, Dubna, Head Post Office, P.O. Box 79, RU-101 000 Moscow, Russian Federation

¹⁷Institut für Experimentelle Kernphysik, Universität Karlsruhe, Postfach 6980, DE-76128 Karlsruhe, Germany

¹⁸Institute of Nuclear Physics and University of Mining and Metallurgy, Ul. Kawiora 26a, PL-30055 Krakow, Poland

¹⁹Université de Paris-Sud, Lab. de l'Accélérateur Linéaire, IN2P3-CNRS, Bât. 200, FR-91405 Orsay Cedex, France

²⁰School of Physics and Chemistry, University of Lancaster, Lancaster LA1 4YB, UK

²¹LIP, IST, FCUL - Av. Elias Garcia, 14-1º, PT-1000 Lisboa Codex, Portugal

²²Department of Physics, University of Liverpool, P.O. Box 147, Liverpool L69 3BX, UK

²³LPNHE, IN2P3-CNRS, Univ. Paris VI et VII, Tour 33 (RdC), 4 place Jussieu, FR-75252 Paris Cedex 05, France

²⁴Department of Physics, University of Lund, Sölvegatan 14, SE-223 63 Lund, Sweden

²⁵Université Claude Bernard de Lyon, IPNL, IN2P3-CNRS, FR-69622 Villeurbanne Cedex, France

²⁶Univ. d'Aix - Marseille II - CPP, IN2P3-CNRS, FR-13288 Marseille Cedex 09, France

²⁷Dipartimento di Fisica, Università di Milano and INFN, Via Celoria 16, IT-20133 Milan, Italy

²⁸Niels Bohr Institute, Blegdamsvej 17, DK-2100 Copenhagen Ø, Denmark

²⁹NC, Nuclear Centre of MFF, Charles University, Areal MFF, V Holesovickach 2, CZ-180 00, Praha 8, Czech Republic

³⁰NIKHEF, Postbus 41882, NL-1009 DB Amsterdam, The Netherlands

³¹National Technical University, Physics Department, Zografou Campus, GR-15773 Athens, Greece

³²Physics Department, University of Oslo, Blindern, NO-1000 Oslo 3, Norway

³³Dpto. Física, Univ. Oviedo, Avda. Calvo Sotelo s/n, ES-33007 Oviedo, Spain

³⁴Department of Physics, University of Oxford, Keble Road, Oxford OX1 3RH, UK

³⁵Dipartimento di Fisica, Università di Padova and INFN, Via Marzolo 8, IT-35131 Padua, Italy

³⁶Rutherford Appleton Laboratory, Chilton, Didcot OX11 0QX, UK

³⁷Dipartimento di Fisica, Università di Roma II and INFN, Tor Vergata, IT-00173 Rome, Italy

³⁸Dipartimento di Fisica, Università di Roma III and INFN, Via della Vasca Navale 84, IT-00146 Rome, Italy

³⁹DAPNIA/Service de Physique des Particules, CEA-Saclay, FR-91191 Gif-sur-Yvette Cedex, France

⁴⁰Instituto de Física de Cantabria (CSIC-UC), Avda. los Castros s/n, ES-39006 Santander, Spain

⁴¹Dipartimento di Fisica, Università degli Studi di Roma La Sapienza, Piazzale Aldo Moro 2, IT-00185 Rome, Italy

⁴²Inst. for High Energy Physics, Serpukov P.O. Box 35, Protvino, (Moscow Region), Russian Federation

⁴³J. Stefan Institute, Jamova 39, SI-1000 Ljubljana, Slovenia and Department of Astroparticle Physics, School of Environmental Sciences, Kostanjevska 16a, Nova Gorica, SI-5000 Slovenia, and Department of Physics, University of Ljubljana, SI-1000 Ljubljana, Slovenia

⁴⁴Fysikum, Stockholm University, Box 6730, SE-113 85 Stockholm, Sweden

⁴⁵Dipartimento di Fisica Sperimentale, Università di Torino and INFN, Via P. Giuria 1, IT-10125 Turin, Italy

⁴⁶Dipartimento di Fisica, Università di Trieste and INFN, Via A. Valerio 2, IT-34127 Trieste, Italy and Istituto di Fisica, Università di Udine, IT-33100 Udine, Italy

⁴⁷Univ. Federal do Rio de Janeiro, C.P. 68528 Cidade Univ., Ilha do Fundão BR-21945-970 Rio de Janeiro, Brazil

⁴⁸Department of Radiation Sciences, University of Uppsala, P.O. Box 535, SE-751 21 Uppsala, Sweden

⁴⁹IFIC, Valencia-CSIC, and D.F.A.M.N., U. de Valencia, Avda. Dr. Moliner 50, ES-46100 Burjassot (Valencia), Spain

⁵⁰Institut für Hochenergiephysik, Österr. Akad. d. Wissensch., Nikolsdorfergasse 18, AT-1050 Vienna, Austria

⁵¹Inst. Nuclear Studies and University of Warsaw, Ul. Hoza 69, PL-00681 Warsaw, Poland

⁵²Fachbereich Physik, University of Wuppertal, Postfach 100 127, DE-42097 Wuppertal, Germany

⁵³On leave of absence from IHEP Serpukhov

⁵⁴Now at University of Florida

1 Introduction

This paper reports on analyses of the fermion-antifermion pair production cross-sections and the leptonic forward-backward asymmetries with the DELPHI data taken during the LEP energy scans of 1993 and 1995, and in 1994 when LEP operated at a single energy near the Z^0 peak. In 1993 and 1995 LEP operated at the peak energy and at 1.76 GeV above and below (the so-called “peak \pm 2” points). Before the scans with carefully monitored energies commenced, data were taken at the peak (the “pre-scan” points). Combining these data with DELPHI results from previous years, allowed values of the Z^0 resonance parameters to be determined with significantly smaller uncertainties than those previously published by DELPHI [1,2]. Lineshape and asymmetry measurements, such as those reported here, constitute major inputs to the tests of the Standard Model and to the determination of its parameters.

This paper is organised as follows. In section 2 we give a brief account of the LEP energy determinations. In section 3 the principal components of the DELPHI detector which are relevant for this analysis are presented, and in section 4 the determinations of the luminosity are described. In section 5 the measurements of the hadronic cross-sections are described, and in sections 6, 7 and 8 the cross-sections and forward-backward asymmetries in the leptonic channels are presented. The $\mu^+\mu^-$ events with a hard initial state photon have been analysed to give measurements of the cross-sections and forward backward asymmetries at centre-of-mass energies between 20 and 87 GeV, and these results are presented in section 9. In section 10 the fits to the data reported here, and all previous DELPHI lineshape and asymmetry data are described and in section 11 the results are interpreted within the framework of the Standard Model. Section 12 contains a summary of the results.

2 Determination of the LEP Energies

Since 1993 the energies of the LEP beams have been routinely measured by resonant depolarization [3] performed typically at the end of a physics fill. Table 1 shows the integrated luminosity for each year and the number of fills where the energy was directly measured at the end. Given that the measurements could not be done for every fill and that they had not been performed under the conditions used for data taking (separated beams and special orbit tuning) a model of the energy behaviour was necessary to provide the experimental energy. This model has to account for the variation of energy during a fill for the calibrated fills and between fills for the fills which were not calibrated at the end. The model has been developed by the Working Group on LEP Energy [4,5] and a file is provided with the estimate for the LEP centre-of-mass energy at the DELPHI interaction point every 15 minutes during a fill, which typically lasted several hours. This is in turn converted to an average energy per cassette of raw DELPHI data.

The model comprises all known sources of variation of the LEP transverse magnetic field, changes of the size of the LEP ring and accelerator effects which can affect the centre-of-mass energies.

The understanding of tidal deformations of the LEP ring is well established. The puzzling variations of the LEP energy over a period of weeks which were first observed in 1993 are now controlled and corrected for by the system of Beam Orbit Monitors of LEP and understood in term of geological stresses of the LEP tunnel due to the pressure of the water table and of the effect of the weight of Lake Geneva on the earth surrounding the LEP ring. In 1995 new Nuclear Magnetic Resonance probes were installed in two dipoles

in the LEP tunnel allowing for the first time a direct monitoring of the magnetic field seen by the beam. Also in 1995 resonant depolarization measurements were attempted routinely at the end of each physics fill. The 6 fills calibrated both at the beginning and at the end showed an unsuspected drift of the beam energy, typically of a few MeV. This effect was also monitored continuously with the NMR probes. The understanding of the energy behaviour of the LEP beams was greatly improved by the ensuing studies. The temperature dependence of the dipole field was studied in great detail in the laboratory indicating a non-linear behaviour more complex than expected. A fluctuating parasitic current of typical magnitude 1A was detected on the beam pipe: a series of experiments identified the source as the leakage from the tracks of a nearby railway line.

In 1993 and 1994 LEP worked in pretzel mode with 8 bunches per beam¹ while in 1995 LEP operated with 4 trains of up to 4 bunches each separated by less than 70m. In this latter mode of operation the unwanted collisions on either side of each interaction point were avoided by separating the beams in the vertical plane. This vertical separation caused a finite vertical dispersion² of opposite sign for each beam. In such situation if the two opposite beams cross with a finite vertical offset a systematic shift of the centre-of-mass energy can occur. These effects have been foreseen and measures taken to maintain them at negligible levels [5]. In 1995, in parallel with the energy scan, LEP started the commissioning of the first complement of Superconductive Radiofrequency Cavities installed to increase the LEP energy. A new model of the RF corrections was developed accordingly; the RF corrections to the centre-of-mass energies in DELPHI are of the order of 1 MeV with a total uncertainty well below 1 MeV [5].

The model was built in a way that the knowledge accumulated in 1995 could be fed back and used to estimate the energy also for 1994 and 1993 [5]. The energies for the bulk of the data collected at the peak in 1994 are known with an accuracy comparable to those of the scan data of 1993 and 1995, due to the relatively high number of calibrations performed. There are datasets collected either before the start of the scan in 1993 and 1995 or in special accelerator conditions at the end of 1994 where the determination of the energy was more difficult due to incomplete records of the accelerator conditions. For these periods an overall centre-of-mass energy uncertainty, typically around 20 MeV, was estimated. For earlier years, when the amount of information recorded was small, the published analysis [6] and its conservatively estimated uncertainties are still adequate.

The various contributions to the uncertainties on the energy estimates are correlated at different levels between years and energy points. In general high correlation between the energy points translates into important uncertainty contributions to M_Z whereas low level of correlation between off-peak points contributes to the uncertainty on σ_Z . The most important uncertainty on M_Z (varying from $\approx \pm 2.5$ MeV for 1993 to $\approx \pm 1$ MeV in 1995) comes from the uncertainty on the modelling of the energy rise during a fill. The largest uncertainty contribution for σ_Z ($\approx \pm 1$ MeV) comes from the fill to fill normalization.

The net effect of the LEP energy uncertainties and their correlations is to give systematic uncertainties, common between the LEP experiments, of ± 1.8 MeV on the mass and ± 1.1 MeV on the width of the resonance, when data from all years and all experiments are combined. The rms energy spread of the beams has been determined [5] empirically to be about 55 MeV and all cross-sections reported here have been corrected for this effect.

¹The unwanted collisions in the middle of the LEP circular sections were avoided by setting the beams into a pretzel-like oscillation in the horizontal plane.

²Spatial ordering of particles according to their momentum.

3 The DELPHI Detector

A detailed description of the DELPHI apparatus and its performance can be found in refs. [7,8]. For the present analysis the following parts of the detector are relevant:

- for the measurement of charged particles the Microvertex Detector (VD), the Inner Detector (ID), the Time Projection Chamber (TPC), the Outer Detector(OD) and the Forward Chambers A and B (FCA and FCB). For the 1995 running a lengthened Inner Detector was installed. The polar angle³ coverage was thereby extended from $23^\circ < \theta < 157^\circ$ to $15^\circ < \theta < 165^\circ$ with a corresponding increase in forward tracking efficiency;
- for the measurement of electromagnetic energy the High-density Projection Chamber (HPC) and the Forward Electromagnetic Calorimeter (FEMC); these detectors were also used for identifying minimum ionizing particles;
- for the measurement of the hadronic energy and muon identification the Hadron Calorimeter (HCAL), which covered both the barrel and endcap regions;
- for muon identification the barrel (MUB) and endcap (MUF), and from the latter part of 1994 onwards, the newly installed and commissioned surround muon chambers (SMC), which complete the polar coverage between barrel and endcap;
- for the trigger, besides the detectors mentioned above, the barrel Time of Flight counters (TOF), the endcap scintillators (HOF) and a scintillator layer embedded in the HPC;
- for the measurement of luminosity (Section 4) the Small Angle Tagger (SAT) and the Very Small Angle Tagger (VSAT) were used in 1993. For the 1994 and later running the SAT was replaced by the Small Angle Tile Calorimeter (STIC).

Data were only accepted for the different measurements when the parts of the detector crucial to them were operating efficiently. Details of the requirements are given in the relevant sections.

The response of the detector to physics processes was modelled using the simulation program DELSIM [8], which incorporates the resolution, granularity and efficiency of the detector components. The event generators chosen for each process are described in the relevant sections of this paper. Simulated data were passed through the same reconstruction and analysis chains as the real data.

4 Determination of the Luminosity

The absolute measurement of the luminosity in 1993 was based on the SAT calorimeter, but the relative luminosity at the off-peak points was taken from the VSAT data, thus making a significant reduction in the statistical uncertainties on the cross-sections. For the 1994 and 1995 running the STIC replaced the SAT.

4.1 The SAT Measurement

The SAT luminosity measurement was based on the observation of small angle Bhabha scattering in calorimeters consisting of lead sheets and plastic scintillating fibres, covering the polar angle range from 43 to 135 mrad. The fiducial volume was accurately defined

³The DELPHI coordinate system has the z -axis aligned along the electron beam direction, the x -axis points toward the centre of LEP and the y -axis is vertical. R is used to measure the radius in the (x, y) plane. The polar angle θ is measured with respect to the z -axis and the azimuthal angle ϕ is about z .

by a precisely machined tungsten mask in front of one of the calorimeters. Due to the narrow width of the transition region from 0 to 85% energy deposition, about 100 μm , a simple energy cut corresponds to the geometrical region covered by the mask. A second mask (the “ ϕ mask”) covered the junction in the vertical plane of the two halves of the masked calorimeter.

For the 1993 running the SAT was equipped with a tracker consisting of 2 planes of silicon strips in front of the calorimeter opposite the masked calorimeter. The use of the tracker data allowed a considerable reduction in the systematic uncertainty due to the definition of the fiducial region in the unmasked calorimeter.

The SAT Bhabha trigger required a coincidence of coplanar energy deposits of greater than 12 GeV, and was measured to have an efficiency of 100% with a statistical uncertainty of 0.01%.

The analysis of the SAT data followed closely those described in refs. [1] and [2]. The event selection criteria which defined the experimental acceptance were:

1. Acoplanarity angle, defined by the beam axis and the showers in each calorimeter, less than 20° .
2. Radial position of the shower in the masked calorimeter less than 31.25 cm.
3. Radial position of the shower in the unmasked calorimeter greater than 12.50 cm.
4. The minimum of the energies in the masked and the unmasked calorimeter greater than 65% of the beam energy.
5. The fraction of the energy of the shower in the masked calorimeter which is in the first readout ring (behind the ring mask) less than 65%.
6. Azimuthal position in the masked calorimeter more than 8° from the vertical junction between the calorimeter half-barrels.

The theoretical visible cross-section was evaluated using the Monte Carlo event generator BHLUMI V4.02 [9]; the intervening material and the detector response were simulated using the GEANT package [10]. The authors of BHLUMI V4.02 have estimated the theoretical uncertainty for a luminometer of similar geometrical acceptance to the SAT at $\pm 0.16\%$. However the SAT analysis uses a combination of acceptance masks, selections on positions of charged particle tracks and on energy. By varying these selections it was checked that the theoretical QED cross-section was stable within the estimated uncertainty. Including the $\mathcal{O}(\alpha)$ electroweak corrections, the theoretical uncertainty on the visible Bhabha cross-section was taken to be $\pm 0.17\%$.

The systematic uncertainty of the SAT luminosity measurement arises principally from the geometrical definition of the masks, the acceptance selections and the sensitivity to the LEP interaction point and beam tilts. As a result of improved energy calibration of the calorimeters the sensitivity to the minimum energy required is much reduced compared to previous analyses [1,2]. The energy distributions (after requiring $E/E_{BEAM} > 0.65$ in the opposite calorimeter) and the minimum energy distribution relative to the beam energy after the final energy calibration are shown in Figures 1(a-c). The luminosity changes by less than 0.1% for variations of the minimum energy cut between the trigger threshold at 0.3 to within 4 standard deviations of the elastic scattering peak at 0.85 as shown in Figure 1(d). Backgrounds arise from $e^+e^- \rightarrow \gamma\gamma(\gamma)$ events and from accidental coincidences of off-momentum electrons. The latter was measured using a delayed Bhabha trigger. The $e^+e^- \rightarrow \gamma\gamma(\gamma)$ background was evaluated using an event generator [11]. The total systematic uncertainty on the luminosity was estimated to be $\pm 0.29\%$, the individual contributions to which are shown in Table 2.

4.2 The VSAT Measurement

The VSAT is a tungsten-silicon calorimeter which consists of four modules located at 7.7 m from the DELPHI interaction point, behind the superconducting quadrupoles (SCQ). Due to the defocusing effect of the SCQ the angular coverage for particles of the beam energy is between 5 and 6.5 mrad in polar angle and approximately 45° in azimuthal angle. The VSAT trigger for Bhabha events requires coincident energy depositions in opposite modules of at least 20 GeV; a delayed Bhabha trigger was used to determine the accidental rate.

For 1994 and 1995 data, the VSAT luminosity was used to check the run to run stability of the STIC measurement, while for 1993 data the VSAT luminosity was used, as in 1991, to determine the relative point-to-point luminosity in the energy scan.

There were three major improvements with respect to 1991 analysis. First, there was a considerable improvement in the simulation, done using the fast simulation program (FASTSIM) described in ref. [1]:

- High statistics extensive simulations of different beam conditions were performed to evaluate the dependence of the Bhabha accepted cross-section on the beam parameter variations and extract the corresponding coefficients, which are needed to correct the luminosity determination with the procedure described in detail in ref. [1].
- Compared with the simulations performed for the analysis of 1991 data, finer and more extended variations of the beam parameters were explored.
- Both BABAMC [12] and BHLUMI [13] generators were used (the comparison between the two computations was found to be very good in the VSAT angular region).
- Each FASTSIM run had larger statistics.
- Finally, different geometrical positions of the four VSAT calorimeters with respect to the beam pipe were tested, within the uncertainty of the survey measurements.

The second improvement was a better understanding of the alignment of the detector with respect to the beam pipe, which is particularly important in the LEP plane (x, z plane). This was obtained by a careful study of the shape of the distributions of the impact points of the two Bhabha electrons on the detector; these distributions were parameterized in terms of a few relevant parameters quite sensitive to the detector alignment. The dependence of these parameters on the variations of the beam spot coordinates was compared between real and simulated data; the alignment which best fitted the data was determined with its uncertainty by adjusting the simulated (x, z) positions of the four VSAT calorimeters with respect to the beam pipe.

The third improvement was the use of a restricted fiducial volume, which had a smaller acceptance than the large fiducial volume used in 1991 analysis (about 78%) but required a considerably smaller correction for the variation of the beam parameters and had a much reduced systematic uncertainty. Two types of events were rejected in the restricted acceptance that had previously been accepted. The first consisted of events in which at least one of the two electrons had an impact point on the detector close to the outer ring of the acceptance (radial distance from the nominal beam axis greater than 7.8 cm). Due to the residual uncertainty in the alignment of the detector with respect to the beam pipe, described above, cutting out these events reduced the corresponding systematic uncertainty at the off-peak points by about a factor 6. In the 1991 data this systematic uncertainty was much smaller because of the smaller spread in the average values of the beam spot x -coordinates and was negligible compared with the other sources of systematic uncertainty. The second selection excluded events in which both electrons were close to the inner edge of the acceptance by requiring that the sum of the absolute values of the

x -coordinates (distances from the beam axis in the horizontal plane) of the impact points of the two electrons be above a given cut. The cut was chosen at the minimum value for which stability in the luminosity determination was obtained. The corresponding uncertainty in the luminosity of the off-peak points was about $\pm 0.02\%$.

Table 3 summarizes the various contributions to the uncertainty for the energy point at peak+2 (the uncertainties are slightly smaller at peak-2 and at the pre-scan point).

As for the 1991 data, the uncertainty due to uncertainties in the correction factors consisted of a part which was almost uncorrelated between different energy points and of a part which was strongly correlated. The latter, for 1993 data, was about $\pm 0.06\%$ and was added quadratically to the VSAT statistical uncertainty at the Z^0 peak ($\pm 0.05\%$) to give the normalization uncertainty to the SAT absolute luminosity. The other uncorrelated systematic uncertainties were convoluted quadratically with the statistical uncertainty at each energy point.

4.3 The STIC Measurement

A second generation luminometer, the STIC (Small Angle Tile Calorimeter) [14], was installed in the DELPHI detector before the 1994 LEP run. It consisted of 2 lead scintillator sampling calorimeters, located at ± 220 cm from the interaction point, providing a full angular coverage in the region between 29 and 185 mrad with respect to the beam line. The scintillating tiles were arranged in towers projecting to the interaction point with 10 radial rings and 16 azimuthal sectors. The absence of cracks pointing to the interaction region and the scheme of light collection provided a very uniform energy response and an excellent energy resolution ($\sigma(E)/E \simeq \pm 2.7\%$ on the Bhabha peak as shown in Figure 2). The uniformity of the energy response and the segmentation of the detector allowed a reconstruction of the radial centre of a shower with a resolution which, at the border between towers, was about $\pm 250 \mu\text{m}$. The way the detector was mechanically assembled resulted in a knowledge of the scintillating tile positions of better than $\pm 50 \mu\text{m}$. Monte Carlo simulations showed that this translates into an effective knowledge of the tower positions of $\pm 20 \mu\text{m}$.

The major improvements with respect to the previous DELPHI luminometer (SAT) can be summarized as follows:

1. The excellent energy resolution allowed for an easy separation of Bhabha scattering events from the background due to off momentum particles from beam-gas interactions.
2. The accuracy in the definition of the internal geometry of the detector, the absence of discontinuities and the good spatial resolution allow a very precise definition of the geometrical acceptance.

During the 1994 data taking STIC worked well, apart from 3 dead tetrodes during the first 5 pb^{-1} , of which only one had an influence on the luminosity measurement. A correction for this effect contributes negligibly to the final systematic uncertainty.

The luminosity was measured with the same “mask technique” used by the SAT. A high precision tungsten mask pointing at the interaction region, with a total thickness of 17 radiation lengths, covered the inner 35 mm of the acceptance of one of the calorimeters. Therefore a cut on the energy of the reconstructed shower translates into a very sharp cut on the inner radius, with an absolute precision of $\pm 20 \mu\text{m}$, as determined by the deviations from circularity of the edge of the mask, which was measured with an accuracy of $\pm 1 \mu\text{m}$. The smearing due to the transition region of the tungsten edge was measured to be 20

μm in a test beam, by using a silicon microstrip detector to define the incoming particle. This is negligible compared to the smearing due to multiple scattering in the beampipe.

The excellent position resolution in the region between two towers means that STIC can provide an independent luminosity determination, entirely based on the reconstructed position of the showers. This was used as a cross-check of the results, as well as for a useful study of the luminosity measurement at LEP II when the mask is not used.

The trigger was based on the same scheme as for the SAT: the analog sum of the signals from 45° azimuthal sectors, each overlapping 22.5° with the neighbouring one, were considered and a coincidence of energy depositions coplanar with the beam in both calorimeters larger than about 9 GeV was required. A prescaled single arm trigger was used to monitor possible trigger inefficiencies, which were found to be smaller than 2×10^{-4} .

In the selection of the Bhabha events only the most energetic clusters on both sides were used.

To remove the background due to off-momentum particles the following cuts were applied:

1. On each side the energy of the cluster was required to be larger than 65% of the beam energy.
2. The acoplanarity between the 2 clusters was required to be less than 20° .

The effect of the energy cut is shown in Figure 3.

A special trigger, requiring a coincidence between the signal from one arm and the delayed signal ($\Delta t = 89 \mu\text{s}$, corresponding to one LEP orbit period) from the other, measured the residual background due to off-momentum particles. This measurement showed that it was smaller than 2×10^{-4} .

To accept radiative Bhabha events, as well as to avoid a strong sensitivity of the accepted cross-section to the beam parameters, the standard technique of an asymmetric acceptance was used.

The following cuts were applied to define the geometrical acceptance:

1. The radial position of the reconstructed cluster was required to be below 25 cm on the tungsten ring side.
2. The radial position of the reconstructed cluster was required to be between 8.2 and 28 cm on the opposite side.

Due to the presence of the tungsten ring, the side with the narrow acceptance was always the same. The variation of the acceptance was equal to 0.1% per mm of longitudinal displacement of the interaction point, while the sensitivity to the transverse position of the interaction point (IP) and to tilts and acollinearities of the beams was much smaller.

Selected collinear Bhabha events allowed a measurement of the average position of the interaction point, on a fill by fill basis, by minimizing the distance of closest approach of the trajectories joining the reconstructed impact points on the calorimeter faces. The typical statistical accuracy for the longitudinal position of interaction point was approximately $150 \mu\text{m}$, using the data from a single fill. A cross-check was performed with the measurement done by the DELPHI tracking system. The difference between the two determinations of the longitudinal position of the interaction point had a standard deviation of $200 \mu\text{m}$.

An accurate estimation of the Bhabha cross-section accepted inside the luminometer was obtained by means of a full simulation of the detector, based on the GEANT [10] program. The simulated events were analysed in the same way as the real data.

The event generator BHLUMI 4.03 [13], which includes the complete $O(\alpha)$, the full leading logs at $O(\alpha^2)$ and the $\gamma-Z$ interference terms was used. The theoretical precision in the calculated cross-section was estimated [15] to be 0.06%.

The total accepted cross-section was estimated to be 54.829 ± 0.010 nb at a centre-of-mass energy of 91.250 GeV.

The contribution of the process $e^+e^- \rightarrow \gamma\gamma$ in the selected sample of Bhabha was calculated to be 0.05%.

A detailed list of the contributions to the systematic uncertainty is given in Table 4. The uncertainty related to the position of the interaction point takes into account the fact that the distance between the two STIC front faces was measured with an accuracy better than $250 \mu\text{m}$. It also takes into account the largest observed variation in temperature measured by the probes located around the STIC modules.

The overall uncertainty is evaluated to be 0.09%, which is better than the design goal of the STIC luminometer. This systematic uncertainty is common to the 1994 and 1995 measurements.

During 1995 the STIC trigger had to be modified in order to cope with the bunch train running of LEP. A correct timing signal for the calorimeter ADC's was made by a coincidence of the wagon gate and the signals coming from the Veto system, which consists of 64 trapezoidal scintillation counters assembled into 2 planes and put in front of the calorimeter.

No wagon assignment was available in 411 out of the 1.6 million Bhabha events taken in 1995 due to inefficiencies of the Veto, and therefore the energy in the STIC was slightly underestimated. In 1.6% of the cases, due to noise in the Veto, the wagon assignment was ambiguous, but the energy in the STIC could be easily corrected offline.

Therefore the contribution of the bunch train operation of LEP to the systematics of the luminosity measurement is negligible.

5 Hadronic Cross-sections

As in previous analyses [1,2] the event selection was based on charged particles only, having momentum greater than $0.4 \text{ GeV}/c$ and polar angle, θ , between 20° and 160° . In order to retain only well measured tracks, those shorter than 30 cm or with momentum resolution larger than 100% were rejected. Events were retained if their charged multiplicity, N_{ch} , was above 4, and if the total energy of the charged particles, E_{ch} , was greater than 12% of the centre-of-mass energy. Bhabha events with multiple reinteractions in the detector material were removed by requiring events with less than 11 charged particles to have E_{rad} ($=\sqrt{(E_f^2 + E_b^2)}$) less than $0.90\sqrt{s}/2$, where $E_{f,b}$ stands for the total energy deposit in the forward and backward electromagnetic calorimeters (FEMC).

The present analysis differs from the previous ones when selecting the tracks with respect to their origin. The determination of the primary vertex of each event was improved, thus allowing the tracks to be selected with tighter cuts: the impact parameter with respect to the vertex position was required to be less than 2 cm in $R\phi$ and less than 4 cm/ $\sin\theta$ in z . A large fraction of the tracks originating from secondary interactions could be eliminated in this way and the residual background from low multiplicity leptonic events could be reduced by up to 50%. As another benefit from the new track selection, the simulation reproduced the real data more accurately and the systematic uncertainty on the selection efficiency was reduced from 0.11% to 0.09%. For those events where the vertex search did not converge, the tracks were selected with respect to the average

position of the beam spot. About 3% of the events were accepted in this way in 1993 and 1995, and about 4% in 1994.

The trigger efficiency was derived from a comparison of independent trigger components based on signals from the tracking detectors, calorimeters or scintillators of the experiment. The efficiency found was higher than 99.99% at all energy points.

The hadronic final states were used to check the stability of the charged particles detectors used for the analysis. The quality of these detectors was estimated for each run from the mean number of tracks and the mean charged energy per event in each detector. Runs where these quantities showed highly abnormal values were discarded from the analysis.

A total of 2,650,000 events was selected over the three years.

The selection efficiency was found from Monte Carlo simulations based on the JET-SET 7.3 generator [16] tuned to DELPHI data [17]. The simulation was carried out for those events in which the generated annihilation energy was greater than $0.1\sqrt{s}$. This cut was introduced explicitly into the fitting procedure used to extract the Z^0 parameters and was estimated to have a negligible effect on the systematic uncertainties. Since the experimental acceptance is zero below this cut, the determination of the Z^0 parameters was therefore insensitive to the theoretical description of the spectrum of low mass hadronic resonances.

The selection efficiency determined from the simulation was corrected for instabilities of the tracking detectors and for detection and tracking inefficiencies in the forward region not included in the simulation. These corrections are shown in Table 5 for each energy point.

The corrected selection efficiency was found to be about 94.8% on the resonance peak in 1993 and 1994. It is largest at peak energies and is smaller by $(0.044 \pm 0.015)\%$ at 89.4 GeV and by $(0.027 \pm 0.015)\%$ at 93.0 GeV because of the variation of N_{ch} and E_{ch}/\sqrt{s} with the collision energy. It was about 0.5% larger in 1995, mainly because of the extension of the acceptance of the Inner Detector in the forward region. The total systematic uncertainty on the 1993 and 1995 selection efficiencies amounts to $\pm 0.09\%$, out of which 0.07% are common to other years. The systematic uncertainty is $\pm 0.10\%$ in 1994, with a part common to previous years amounting to 0.08%. As an example, the different contributions to the systematic uncertainties obtained in 1995 are reported in Table 6.

The influence of the bunch train operation of the LEP collider on the response of the tracking and luminosity detectors, as well as on the track reconstruction efficiency, was investigated. The cross-sections corresponding to each bunch number were extracted. The values obtained, relative to the total cross-section at each collision energy in 1995 are shown in Figure 4. No significant variation of the cross-sections with the bunch number was observed.

The $\tau^+\tau^-$ and e^+e^- backgrounds were evaluated from simulations based respectively on the KORALZ [18] and on the BABAMC [12] generators, and by inspection of distributions sensitive to the residual contaminations (see ref. [1]). These distributions showed that the simulated backgrounds were underestimating the observed ones. The magnitude of each simulated background was then rescaled in order to achieve agreement between the simulated and the real distributions. The $\tau^+\tau^-$ background was found to be about $(0.4 \pm 0.03)\%$ at all energies. The e^+e^- background was typically $(0.07 \pm 0.02)\%$ at 89.4 GeV and $(0.03 \pm 0.01)\%$ at 91.2, 91.3 and 93.0 GeV. The two-photon collision background was estimated to be 16 ± 3 pb from Monte Carlo simulations based on the TWOGAM generator [19], accounting for all three components of the process (i.e. QCD, QPM and

VDM). The systematic uncertainties related to the residual backgrounds are summarised in Table 6.

In Figure 5, the events selected in 1994 at the peak energy are compared to simulated samples of the $q\bar{q}$ signal and of all relevant backgrounds. The charged multiplicity is shown as well as two background sensitive distributions; the acollinearity between the momenta of both event hemispheres, and the Major value. The Major M is defined as

$$M = \max_{\vec{n}_M} \frac{\sum_i |\vec{p}_i \cdot \vec{n}_M|}{\sum_i |\vec{p}_i|}$$

where \vec{p}_i is the momentum vector of charged particle i and \vec{n}_M is the direction which maximizes the momentum sum transverse to the thrust axis. Above the cut values the combined signal and background distributions reproduce the data adequately.

The selection efficiencies and residual backgrounds found at peak energies are summarised in Tables 11, 12 and 13. The hadronic cross-sections measured in 1993, 1994 and 1995 are given in Table 7. Data from a short period in 1994 when the beam energy was significantly different have been treated separately.

6 Cross-sections and Forward-Backward Asymmetries in the e^+e^- Channel

6.1 Selection Criteria

Two different methods were used for event selection, as described in ref. [2]. Only the barrel region of DELPHI was used for this analysis. In each method, both the electron and the positron were required to be within the range $44^\circ < \theta < 136^\circ$, where θ was the polar angle of the particle with respect to the direction of the electron beam, and the acollinearity was required to be smaller than 10° . Due to the influence of the t-channel contribution to e^+e^- scattering, the barrel angular region is the most sensitive to the electroweak parameters.

Runs were excluded where the luminometers had problems, where the hadronic analysis indicated severe problems in the data taking, and where the beam energy was abnormal.

6.1.1 Method 1

This method largely relies on the energy measured in the HPC. Due to the presence of about 0.7 radiation length of material in front of the HPC, electrons have a high probability to radiate before reaching the calorimeter. To obtain the complete reconstruction of the electromagnetic energy, clusters were constructed in the calorimeter by selecting the two most energetic electromagnetic showers in opposite hemispheres and adding to these showers the energy released in the electromagnetic calorimeter in a cone of half-angle 5° around the shower direction, or having a transverse energy, with respect to the most energetic shower, smaller than 0.2 GeV. Charged particles were selected by requiring:

- momentum greater than 1.5 GeV/ c ;
- impact parameter to the average interaction point smaller than 5 cm both in the radial and in the beam direction;
- track length greater than 30 cm.

The association between the charged particle track and the electromagnetic shower was not explicitly required. The direction of the charged particle track or, in case it was missing, the direction defined by the electromagnetic shower centroid and the mean beam position, was used as the fermion direction. Events were divided into two hemispheres defined by the plane perpendicular to the most energetic electromagnetic cluster direction. In order to recover information about tracks which could have deteriorated in the region after the VD, an algorithm was developed to reconstruct “track segments”, independently from the global track search, by using hits in the three VD layers. Events were accepted if they fulfilled one of these two sets of requirements:

- two energy clusters in opposite hemispheres, at least one with energy above 30 GeV, the other above 25 GeV;
- no more than 4 charged particles and, for topologies with more than two tracks in one hemisphere: total electromagnetic energy greater than 70 GeV;
- for topologies with less than two tracks: VD hits compatible with one charged track segment per hemisphere;

or

- one energy cluster with energy above 40 GeV;
- one charged particle in each hemisphere;
- no energy deposited beyond the first 1.5 interaction lengths of the Hadron Calorimeter.

The energy cuts quoted were used at the peak energy and were scaled according to the event centre-of-mass energy at the other scan points. To avoid the region in polar and azimuthal angle where poor efficiency is expected for electromagnetic energy (and track) reconstruction, both fermions were required to be outside the polar range $88^\circ < \theta < 92^\circ$ and at least one was required to be outside $\pm 0.7^\circ$ in ϕ from the HPC gaps between modules.

The selection efficiency was estimated by using events generated with the BABAMC [12] program to be $(89.34 \pm 0.10)\%$, $(89.57 \pm 0.10)\%$ and $(89.77 \pm 0.10)\%$ in the 1993, 1994 and 1995 data respectively. The loss of events was mainly due to the azimuthal fiducial cuts. The selection efficiency was found to be independent of the centre-of-mass energy, within the uncertainties of the Monte Carlo generation.

The main background was due to $\tau^+\tau^-$ events and was estimated by using simulated $\tau^+\tau^-$ events, produced with the KORALZ [18] generator. In the θ acceptance region, the percentage of $\tau^+\tau^-$ events passing the selection cuts was $(1.38 \pm 0.04)\%$, $(1.18 \pm 0.05)\%$, and $(1.24 \pm 0.04)\%$ in 1993, 1994 and 1995 runs respectively, with negligible dependence on the centre-of-mass energy.

6.1.2 Method 2

In this method, e^+e^- events were selected with two almost independent sets of experimental cuts, chosen in such a way as to minimize the correlations between the two sets. As in method 1, a cut in polar angle at $90 \pm 2^\circ$ was applied. In one set (selection A), events were accepted if they had :

- at least two track segments in opposite hemispheres seen by the VD and no more than four in total; events with 2 track segments in each hemisphere were excluded to reject photon conversions;
- two high energy electromagnetic clusters observed in the HPC, at least one with energy above 75% of the beam energy and another above 55% .

In the second set (selection B), events were accepted if they had:

- at least 2 charged particle tracks, of momentum greater than $1.5 \text{ GeV}/c$ and distance of closest approach to the nominal vertex position less than 5 cm, seen by the DELPHI tracking system (except VD) with acollinearity less than 10° , and no more than four tracks in total; the 2-versus-2 track topology was excluded;
- the quadratic sum of the momenta of the highest momentum charged particles in each hemisphere greater than $0.99\sqrt{s}/2$;
- the ionization, as measured by the TPC, of all tracks in the event compatible with the electron hypothesis;
- no energy observed in the last three layers of HCAL associated to the impact points of the two highest momentum charged particles;
- the OD hit pattern associated to the impact points of the tracks compatible with the pattern of a particle showering in or before the OD, or giving back-scattering from the calorimeter;
- no hit in the muon chambers associated to the tracks.

Considering the selections A and B as independent, the efficiency of each of them and the overall efficiency of the “OR” of the two could be easily computed by a comparison of the number of events selected by each one separately or by both simultaneously. To get a correct result, the contribution of background events passing the cuts had first to be subtracted. The presence of background in the sample of selected events had two consequences. First, it increased the number of selected events, second it biased the estimate of the selection efficiency towards smaller values. Using $\tau^+\tau^-$ simulated events the background in the “OR” of the selections was estimated to be $(1.10 \pm 0.04)\%$, $(0.83 \pm 0.04)\%$ and $(0.85 \pm 0.04)\%$ in 1993, 1994 and 1995 runs respectively. In 1994, as an example, it was $(0.49 \pm 0.03)\%$ for selection A only, $(0.53 \pm 0.03)\%$ for selection B only, and $(0.05 \pm 0.01)\%$ for the “AND” of the two selections. After the background correction, the overall efficiency of the two selections was measured to be $(97.82 \pm 0.07)\%$, $(96.95 \pm 0.06)\%$ and $(97.42 \pm 0.08)\%$ in 1993, 1994 and 1995 runs respectively. The simulated e^+e^- events were used to estimate and remove the bias caused by the correlation between the two selections due to the detector structure or to the kinematics of the events. The bias on the combined efficiency was found to be 0.1%. The stability in the estimated total number of events with respect to variations of the cuts is shown in Figure 6. The stability was found to be better than 0.20%.

In both methods the measured efficiencies did not include the loss due to the exclusion of the polar angle region around 90° .

6.2 Measurement of the Cross-section

Totals of 24,286, 41,290 and 20,833 events were selected with Method 2 in 1993, 1994 and 1995 data respectively. A correction was applied for the $\pm 2^\circ$ polar angle fiducial cut around 90° . It was computed at the different energies by using the program TOPAZ0 [20] and checked with ALIBABA [21]. No significant difference was found between the two generators. The total cross-sections obtained with the two selection methods were compatible and the arithmetic average of the two results was used. Since the two samples are highly correlated, there was no reduction in the statistical uncertainty. In order to fit the results with the ZFITTER [22] package, the t-channel contribution had to be removed from the measured cross-sections and asymmetries. This subtraction was computed using the ALIBABA program. Recent studies [23] indicate that the theoretical uncertainty on

this subtraction, averaged over the different energies, amounts to 1.1 pb and 0.3 pb on the forward and backward cross-sections respectively.

In addition, a correction was applied because ZFITTER only allows a limit on the polar angle of one of the two final state fermions, the other being constrained by the collinearity requirement. This correction was calculated using TOPAZ0, and the theoretical uncertainty on the correction was estimated to have a mean value of 0.15% of the s-channel cross-section.

After the subtraction of the t-channel contribution and the correction for the polar angle definition by the electron only, the cross-sections given in Table 8 were obtained. The uncertainties quoted are statistical only. Apart from the luminosity, systematic uncertainties arise from the event selection, acceptance definition and from the t-channel and background subtractions. The systematic uncertainties are shown in Tables 11, 12 and 13 for the different run periods. Of the total systematic uncertainties, 82% are assumed to be correlated between the different years.

As a cross-check, in this analysis, and in the other leptonic analyses, for each running period the stability of the cross-section versus time was investigated by calculating cross-sections for each LEP fill. In addition, for the 1995 run period where LEP was operated in bunch train mode the stability versus the bunch number was studied. No evidence of any systematic dependence was found.

6.3 Measurement of the Forward-Backward Asymmetries

In the samples of events selected with the two methods described above, the charge of the event was defined as positive when the positron was in the forward hemisphere, negative in the opposite case. The method used to determine the charge was similar to the one used for the analysis of the 1992 data [2]. In the $e^+e^- \rightarrow e^+e^-$ events, in addition to the canonical charge definition from reconstructed tracks, it is possible to look at the effects of the magnetic field bending on the impact position of HPC clusters. It is then possible to correlate the sign of the bending with the sign of the event charge, allowing a high redundancy on the charge determination. The percentage of events with two charged particles of the same sign was about 2% of the two-track events. The use of the bending to determine the charge of those events and the charge of the events with more or less than two tracks, avoids possible hemisphere dependent biases. The measured event charge was compared with the generated one in Monte Carlo events, showing a discrepancy in 0.4% of the events, with no evidence of systematic hemisphere bias.

The forward-backward asymmetries were determined with a counting method using the same samples of events considered for the cross-section determination and are given in Table 8 with their statistical uncertainties. Systematic uncertainties arise because of charge confusion, forward-backward acceptance differences and t-channel subtraction. They are shown in Tables 11, 12 and 13 for the different run periods.

7 Cross-sections and Forward-Backward Asymmetries in the $\mu^+\mu^-$ Channel

7.1 Selection Criteria

The same selection criteria were applied for all periods of data taking 1993 - 1995, with minor differences to account for year-to-year changes in detector performance.

The following kinematic, topological and muon identification cuts were applied to obtain a sample of $e^+e^- \rightarrow \mu^+\mu^-$ events with high efficiency and small remaining background:

- The two most energetic charged particles were required to have momenta $P_1, P_2 > 5$ GeV/c. These were defined as the candidate tracks for the subsequent selection;
- To suppress $\tau^+\tau^-$ contamination the event variable P_{rad} , defined as $\sqrt{(P_1^2 + P_2^2)}$, was required to exceed $0.87\sqrt{s}/2$;
- The acollinearity of the two candidate tracks was required to be less than 20° ;
- In events where the two candidate tracks were of opposite charge, the negative particle was required to lie within the polar angle interval $20^\circ - 160^\circ$ for the cross-section measurement. (In the rare occurrence of both tracks having the same charge, a unique μ^- candidate was defined by comparing the assigned momentum uncertainties of both tracks. The charge of the track with the smaller momentum uncertainty was taken as correct.) This was extended to $11^\circ - 169^\circ$ for the asymmetry determination;
- Both candidate tracks had to be identified as muons, requiring an associated hit in the muon chambers (MUB, MUF and, from the latter part of 1994 onwards, the SMC) or energy depositions in the HCAL, the HPC or the FEMC consistent with a minimum ionizing particle. Furthermore the calorimeters were used to reject Bhabha events and tracks from hadrons;
- To reduce the background from cosmic rays, at least one candidate track was required to originate from close to the beam spot at the perigee in the transverse plane. The cut applied depended on the detectors participating in the track reconstruction, but was 0.1 cm for the majority of cases. A cut was also placed on the axial separation of the two tracks at this point.

For the asymmetry analysis of the 1993 pre-scan period, problems with the Forward Chambers A necessitated restricting the polar interval to $18^\circ - 162^\circ$. In all years, events lying within 2° of the six TPC azimuthal sector boundaries were excluded from the asymmetry measurement, as there was evidence of possible bias in these regions. Furthermore the $\sim 0.5\%$ of events in which the charge assignment was the same sign for both tracks were discarded in the asymmetry analysis.

Runs in which relevant components of the DELPHI detector were not adequately operational were excluded from the analysis. For the cross-section analysis this involved a combination of the TPC, the HCAL and the muon chambers. In addition, runs were excluded where the luminometers had problems, where the hadronic analysis indicated severe problems in the data taking, and where the beam energy was abnormal. As the analysis of the forward-backward asymmetry is less dependent on knowledge of detector efficiencies, a looser run selection was used here. Only runs in which the TPC was not fully operational were excluded, although in 1993 further requirements were placed on the muon identification detectors to eliminate a possible detector bias.

Tables 11, 12 and 13 show the number of events remaining for the analyses after all cuts for the different run periods.

7.2 Measurement of the Cross-section

7.2.1 Determination of selection efficiencies

As far as possible, corrections were determined from the data, using input from simulations only for the studies of correlations and for small corrections. This is possible

because of the distinctive back-to-back event topology of $\mu^+\mu^-$ events, and because the DELPHI trigger only requires single tracks.

The important contributions to the selection efficiency which can be determined primarily from the data are the following:

- **Trigger efficiency**

This was measured by comparing independent subtriggers. The event efficiency was $> 99.5\%$ for all years.

- **Muon identification efficiency**

The principal method used a restricted event sample with negligible $\tau^+\tau^-$ and Bhabha background. The event efficiency was found to be $> 99\%$ throughout the acceptance, except between the barrel and the forward regions for the data collected before the installation of the SMC.

- **Tracking efficiency**

A loss of $\sim 3\%$ near the sector boundaries of the TPC was determined from the azimuthal distribution of events. Away from these boundaries an efficiency of $> 99.5\%$ was calculated by use of an event sample with one identified muon track plus a hit in the muon chambers in the opposite hemisphere.

These efficiencies were measured and then combined in polar angle bins to account for angular correlations. Systematic uncertainties were assigned from comparison of various tracking detectors and from the statistical precision of the measurements.

Further losses, such as those due to vertex cuts and background vetoes were measured through a combination of data and simulations. The loss due to the P_{rad} cut was studied with a variety of event generators and found to be $< 0.1\%$.

The total selection efficiencies for the different running periods are given in Tables 11, 12 and 13. These are with respect to events within the polar, momentum and acollinearity acceptance stated above. Uncertainties in the detector implementation of this acceptance are included in the assigned uncertainty. Figure 7 shows the behaviour of the selection efficiency as a function of the polar angle for the 1994 running period.

7.2.2 Determination of residual backgrounds

The residual contamination from $\tau^+\tau^-$ events was determined by fitting the relative contribution of $\mu^+\mu^-$ and $\tau^+\tau^-$ events in discriminant variables. The best sensitivity was obtained by fitting in P_{rad} , as illustrated in Figure 8. The residual $\tau^+\tau^-$ contamination was found to be $\sim 1\%$.

The background from cosmic muons was determined from data, by counting the number of events failing the impact parameter cuts and interpolating to the region within the cuts. This gave a contamination of $\sim 0.1\%$. Cross-checks using detectors with timing and directional information, such as the RICH, confirmed this result.

Contamination from other backgrounds, such as from two-photon processes and from Bhabha events was found to be of order 0.01% and therefore negligible in the measurement.

The background estimates for the three years are summarised in Tables 11, 12 and 13.

7.2.3 Results

The resulting cross-sections after subtraction of backgrounds and correction for inefficiencies are given in Table 9. These numbers are given within the phase space defined by a cut of $5 \text{ GeV}/c$ on the momentum of the outgoing particles, an acollinearity cut of 20°

and a restriction of the polar angle of the negatively charged muon to $20^\circ - 160^\circ$. The systematic uncertainty does not include the uncertainty due to luminosity measurement. The differential cross-sections combined for all years 93 - 95 are shown in Figure 9.

7.3 Measurement of the Forward-Backward Asymmetry

The forward-backward asymmetry was calculated using an unbinned maximum likelihood fit to the lowest order form of the angular distribution. In such a fit the result is insensitive to knowledge of the selection efficiencies, provided that these are the same for events with forward going negative muons and backward going negative muons.

In order to bias the asymmetry measured using the likelihood method, it is necessary to suffer from forward-backward asymmetric *and* charge asymmetric efficiencies. To test the assumption of symmetry, the detector asymmetry, A_{det} , was determined for each running period. This is defined as follows:

$$A_{det} = \frac{\epsilon_{fwd}^- \epsilon_{bwd}^+ - \epsilon_{bwd}^- \epsilon_{fwd}^+}{\epsilon_{fwd}^- \epsilon_{bwd}^+ + \epsilon_{bwd}^- \epsilon_{fwd}^+}, \quad (1)$$

where ϵ_{fwd}^{+-} and ϵ_{bwd}^{+-} are the efficiencies to reconstruct a μ^+/μ^- in the forward or backward hemisphere of the detector respectively. Evidence of non-zero detector asymmetry was found around the azimuthal TPC sector boundaries, and in the very forward region during the 1993 pre-scan. With these regions excluded, A_{det} was found to be compatible with zero for all periods. For each data set the statistical uncertainty on this conclusion was assigned as the systematic uncertainty. This dominated other uncertainties, but was still small compared to the statistical uncertainty. Figure 10 shows the detector asymmetry as a function of the polar angle for the running period of 1994.

Further sources of systematic uncertainties that have been considered include the biases induced by $\tau^+\tau^-$, cosmic and Bhabha contamination, possible uncertainties in the measurement of the polar angle, a charge dependence of the momentum determination, and the exclusion of events with at least one misassigned charge. The effect of neglecting higher order terms in the form of the angular distributions was investigated and found to be small.

The stability of the forward-backward asymmetry against time was tested by calculating its value separately for each LEP fill. Also the asymmetry was determined in bins of the polar angle, to look for any residual systematic effects. These checks showed no problems.

The forward-backward asymmetries and the assigned systematic uncertainties are given in Table 9 within the phase space defined by a cut of 5 GeV on the momentum of the outgoing particles and an acollinearity cut of 20° .

8 Cross-sections and Forward-Backward Asymmetries in the $\tau^+\tau^-$ Channel

8.1 Selection criteria

The selection of $\tau^+\tau^-$ events in the barrel region of the detector from the 1993-1995 data was similar to that described in ref. [2]. In addition, the analysis has been extended to include data in the forward regions of the detector and for the first time with DELPHI data the $\tau^+\tau^-$ cross-section has been measured in the polar angle range $20^\circ < \theta < 160^\circ$.

The same selection criteria were applied to the entire sample, with minor differences to account for year-to-year changes in detector performance.

Events were required to be of low multiplicity and to have high thrust, in order to remove background from $q\bar{q}$ final states. Further kinematic restrictions were imposed to remove the backgrounds from e^+e^- , $\mu^+\mu^-$ and four-fermion final states. For the barrel selection the thrust axis, computed using charged particle momenta, was required to lie in the polar angle interval $43^\circ < \theta < 137^\circ$. Events were also rejected if the highest momentum charged particles in each event hemisphere were both in the polar angle range $88^\circ < \theta < 92^\circ$. The following topological and kinematic cuts were applied:

- The number of well reconstructed charged particle tracks per event, N_{ch} , was required to be in the range $2 \leq N_{ch} \leq 6$;
- The event thrust was required to exceed 0.996;
- To suppress $\mu^+\mu^-$ contamination, the event variable P_{rad} (see section 7.1) was required to satisfy $P_{rad} < \sqrt{s}/2$;
- To suppress e^+e^- contamination, the event variable E_{rad} , defined as $\sqrt{(E_1^2 + E_2^2)}$, where E_1 and E_2 are the energies in the electromagnetic calorimeters within a cone of half-angle 30° around the thrust direction in each hemisphere, was required to satisfy $E_{rad} < \sqrt{s}/2$;
- To suppress four-fermion final states, the total charged and neutral energy, E_{vis} , was required to exceed $8\sqrt{s}/91.2$ GeV;

Additional cuts were imposed on those events with $N_{ch} = 2$ to reduce further the backgrounds from Bhabha scattering and cosmic muons. The former were most effectively removed by requiring that the acollinearity angle exceed 0.5° and the latter were almost entirely eliminated with tight cuts on the track impact parameters with respect to the beam collision point in the $R - \phi$ plane.

For the 1993 data, in order to avoid a possible selection efficiency bias due to poor modelling of the electron momentum spectrum, the P_{rad} cut was only applied to those events which satisfied a very loose $\mu^+\mu^-$ event selection based on muon chamber and calorimeter information. In the absence of this cut, the e^+e^- background was removed by imposing harder E_{rad} cuts: $E_{rad} < 0.9\sqrt{s}/2$ and $E_{rad} < 0.6\sqrt{s}/2$ for those events in which the track of the highest momentum particle in either thrust hemisphere passed close ($\pm 1.5^\circ$) to one of the 24 azimuthal boundary planes between adjacent HPC modules.

For the 1995 data, in order to avoid biases due to imperfect modelling of the E_{rad} distribution, events were required to satisfy $E_{rad} < 0.95\sqrt{s}/2$ if the highest momentum charged particle in each event hemisphere passed more than 0.3° from the nearest HPC azimuthal boundary. For events in which only one of these highest momentum charged particles passed more than 0.3° from the nearest HPC azimuthal boundary this requirement was tightened to $\sqrt{s}/3$. Due to improvements in the Vertex Detector and Inner Detector performance in 1995 the impact parameter cuts were much more effective in removing the cosmic muon background.

Events in the forward region were selected by requiring that the thrust axis fell in the polar angle ranges $20^\circ < \theta < 43^\circ$ or $137^\circ < \theta < 160^\circ$. The majority of the cuts used in the barrel event selection were also employed in the forward region, but with several significant changes in order to suppress background, especially from Bhabha scattering:

- To suppress four-fermion background⁴, E_{vis} was required to exceed $12\sqrt{s}/91.2$ GeV;

⁴The four-fermion background is the set of four-fermion final states which are not included as part of the radiative corrections to the ZFITTER cross-section for the $\tau^+\tau^-$ final state; the dominant contribution to this background arises from two-photon collision processes.

- The Bhabha background was severely limited by restricting the acollinearity angle between the tracks in opposite thrust hemispheres to be greater than 1° over most of the angular range, or 2° in the polar angle range $35^\circ < \theta < 43^\circ$ or $137^\circ < \theta < 145^\circ$. For events with more than two charged particle tracks the acollinearity was determined using the vector sum of the charged particle momenta in each thrust hemisphere;
- To restrict further the Bhabha background, harder E_{rad} cuts were imposed: $E_{rad} < 0.8\sqrt{s}/2$, or $E_{rad} < 0.6\sqrt{s}/2$ if the thrust axis was in the range $35^\circ < \theta < 43^\circ$ or $137^\circ < \theta < 145^\circ$. In these ranges of angles the electromagnetic calorimetry was relatively poor.

For the analysis of the 1995 data in the forward region the E_{rad} and P_{rad} requirements were altered. If the highest momentum charged particle in each event hemisphere extrapolated to within the acceptance of the FEMC, the E_{rad} cut was $0.85\sqrt{s}/2$. If only one of these tracks extrapolated to the FEMC then the cut was tightened to $0.4\sqrt{s}/2$. The P_{rad} cut was reduced to $0.9\sqrt{s}/2$ in both cases.

A run selection was applied to exclude runs from the analysis in which the relevant components of the DELPHI detector were not adequately operational. For the cross-section analysis this involved a combination of the TPC and the HPC. In addition, runs were excluded where the luminometers had problems, where the hadronic analysis indicated severe problems in the data taking, and where the beam energy was abnormal. For the asymmetry analysis the requirements on the luminometer performance were dropped.

Tables 11, 12 and 13 show the number of events remaining in each year after the application of the selection criteria.

8.2 Measurement of the Cross-section

8.2.1 Determination of selection efficiencies

The determination of the event selection efficiency for $\tau^+\tau^-$ is highly dependent on Monte Carlo simulation (using the KORALZ program [18]) because the selection criteria are based on the use of a number of global event variables such as E_{rad} and P_{rad} . This contrasts with the e^+e^- and $\mu^+\mu^-$ analyses which treat the reconstruction and identification of each lepton independently. Consequently, the event reconstruction and identification efficiencies do not factorize. The trigger efficiency can, however, be determined from the experimental data by comparing independent subtriggers, and in all years it exceeded 99.9%.

The quality of the Monte Carlo modelling of the $\tau^+\tau^-$ events was monitored by comparing distributions of experimental data and simulated data (including residual background contributions) in all of the topological and kinematic variables used for the event selection. Figures 11 and 12 show such comparisons for the event thrust distribution and for the radial energy variable, E_{rad} . A small discrepancy in the modelling of the reconstruction efficiency for tracks close to the six azimuthal TPC boundary planes was observed and a small correction ($< 1.0\%$) was applied to the event selection efficiency.

The combined event selection efficiency for the barrel and forward regions was determined by simulation to be in the range 62% – 64% for the three running periods. The trigger and selection efficiencies for the different running periods are given in Tables 11, 12 and 13.

8.2.2 Determination of residual backgrounds

The main backgrounds in the selection of $\tau^+\tau^-$ arise from $q\bar{q}$, e^+e^- , $\mu^+\mu^-$ and four-fermion final states. Each contribution was determined by Monte Carlo simulation. For the $q\bar{q}$ and $\mu^+\mu^-$ backgrounds the JETSET 7.3 [16] and DYMU3 [24] generators were used respectively. The two-photon backgrounds were simulated using the TWOGAM [19] and BDK [25] generators. The residual level of the Bhabha background was studied using two Monte Carlo generators: BABAMC [12] and BHWIDE [26]. It was found that the BHWIDE generator predicted about 1 pb more background than BABAMC in terms of the accepted cross-section. This resulted in about 0.001 increase in the observed forward-backward asymmetry. Since BHWIDE is expected to be more precise, its prediction was used to subtract the residual background, and half the difference between the two generators was added to the systematic uncertainty on the cross-section and forward-backward asymmetry.

Various discriminating variables were used to check that the experimental data and simulated data were consistent. For example, the E_{rad} distribution (see Figure 12) is sensitive to the e^+e^- background whereas the P_{rad} distribution is sensitive to the $\mu^+\mu^-$ background.

The only other significant residual background, from cosmic muons, was determined from the experimental data using the technique applied in the $\mu^+\mu^-$ event selection (see section 7.2.2) based on impact parameter distributions.

The backgrounds for the different running periods were quite similar but with some variation due to the change of cuts after 1993. As an illustration of typical magnitudes, the 1995 background levels were as follows. The four-fermion background was estimated to be 2.64 ± 0.32 pb, that due to $q\bar{q}$ events $(1.10 \pm 0.15)\%$ and that due to $\mu^+\mu^-$ events $(0.25 \pm 0.05)\%$ at all energies. The cosmic muon background was estimated to be 0.2 ± 0.1 pb at all energies and the e^+e^- background to be 7.8 ± 0.9 pb, 11.2 ± 1.2 pb and 7.6 ± 0.9 pb, at the centre-of-mass energies of 89.4 GeV, 91.2 GeV and 93.0 GeV respectively. The total background at the Z peak was 2.9% of the selected event sample. Tables 11, 12 and 13 show the various background estimates for the different running periods.

8.2.3 Results

The resulting cross-sections after subtraction of backgrounds and correction for inefficiencies are given in Table 10. These numbers are given fully corrected for the effects of kinematic and acceptance cuts. A comparison of the τ -pair invariant mass spectrum revealed a discrepancy between the KORALZ and ZFITTER [22] programs at low values of the τ -pair invariant mass. The former program⁵, used to compute the event selection efficiency, was found to be in error in this small mass region. Consequently a small correction, amounting to 4.5 pb, was applied to the measured cross-sections at each centre-of-mass energy for each year.

The systematic uncertainty due to selections and backgrounds is estimated to be $\pm 0.6\%$ for all running periods, in addition to the systematic uncertainty on the luminosity. The differential cross-sections for 1995 are shown in Figure 13.

8.3 Measurement of Forward-Backward Asymmetry

The forward-backward asymmetry was calculated using an unbinned maximum likelihood fit to the lowest order form of the angular distribution. As remarked in section 7.3,

⁵The version 3.8 of KORALZ was used for the simulation. The small discrepancy has been corrected in later versions.

such a fit is expected to be insensitive to knowledge of the event selection efficiencies. The fit was performed on the events in which the numbers of tracks in each hemisphere were 1–1, 1–3 and 3–3 in the polar angle range $20^\circ < \theta < 160^\circ$. For the 1995 data an alternative topological selection was studied in which 1–N events were used in the fit (N=1,..5). The results were found to be consistent with those obtained with the standard topological selection.

Systematic uncertainties arise from the e^+e^- subtraction, from charge confusion and from neglect of radiative corrections which alter the lowest order angular distribution. A small additive correction (less than 0.003 in magnitude) has to be made to the measured asymmetry to account for biases introduced by the selection cuts. These biases arise from initial state radiation and from the θ dependence of the τ polarization. The precise value of this correction depends on the cuts used, which varied from year to year and between the barrel and forward region, and was determined by Monte Carlo simulation. The uncertainty on the correction of ± 0.0009 was dominated by Monte Carlo statistics. The overall systematic uncertainties are estimated to be ± 0.005 , ± 0.002 and ± 0.002 at centre-of-mass energies of 89.4 GeV, 91.2 GeV and 93.0 GeV respectively. The forward-backward asymmetries measured in each running period appear in Table 10.

Table 14 gives for the different years the correlation coefficients between the systematic uncertainties in the cross-section determinations in the hadronic and leptonic channels. The systematic uncertainties in the luminosity determination are not included. Similarly, Table 15 gives the correlation coefficients of the systematic uncertainties in the determinations of the leptonic forward-backward asymmetries.

9 Cross-sections and Forward-Backward Asymmetries in the $\mu^+\mu^-$ Channel with Initial State Radiation

Experimental results from studies of events collected at LEP1 in the channel $e^+e^- \rightarrow \mu^+\mu^-\gamma_{\text{ISR}}$, with γ_{ISR} being a photon radiated from the initial state, have been used to probe the cross-sections and forward-backward asymmetries in the energy region between LEP1 and TRISTAN and down to PETRA energies. Similar measurements have been performed previously by DELPHI [27] with the data taken between 1991 and 1994, and by other experiments [28]. In this section the analysis of the data taken in 1995 is presented. By adding these data to those taken between 1991 and 1994, cross-sections and forward-backward asymmetries were determined as well as the helicity cross-section ratio $\frac{\sigma_{LL}+\sigma_{RR}}{\sigma_{RL}+\sigma_{LR}}$ where the two subscripts stand for the helicities of the incoming e^- and outgoing μ^- respectively. The theoretical background to these analyses is explained in refs. [27] and [29].

For the simulation studies about 220,000 dimuon events were generated with the DY-MU3 program [24] at the same 3 energies as the data, about 103,000 $\tau^+\tau^-$ events were generated with the KORALZ program [18] and about 25,000 $e^+e^- \rightarrow e^+e^-\mu^+\mu^-$ events were generated with the FERMISV program [30]. All generated events were passed through the detector simulation program DELSIM [8] and the same event reconstruction program as the data.

9.1 Selection of events

The selection of dimuon events with Initial State Radiation (ISR) from the data taken in 1995 was performed as described in ref. [27]. First a sample of dimuon events with or without photon production was selected for normalisation purposes. From this sample the events with ISR were then extracted. For the calculation of the cross-sections, the same selection procedure was applied to the 220,000 simulated dimuon events.

To select the sample of dimuon events allowing for possible photon emission, the events had to contain two charged particles of momentum greater than 10 GeV, both of which were identified as muons either by the muon chambers, by the hadron calorimeter or by the electromagnetic calorimeters. Both particles had to come from the interaction region, which was defined as $|z|$ less than 4.5 cm and R less than 1.5 cm. The variable $P_{rad} = \sqrt{P_1^2 + P_2^2}$, where P_1 and P_2 are the momenta of the two muons, had to exceed $0.3\sqrt{s}/2$. Events with more than 5 charged particle tracks were rejected.

To reduce the $\tau^+\tau^-$ background, three criteria were introduced. Firstly, if the acollinearity angle between the two muons was larger than 1° , the event was rejected if the energy deposited in the hadron calorimeter was larger than a cutoff value dependent on the polar angle (see [1]). Secondly, if the event had more than 2 charged particle tracks, either the acollinearity angle between the two muons had to be less than 1° or both muons had to have at least one associated hit in the muon chambers. Thirdly, in the procedure to separate ISR from Final State Radiation (FSR) events, a variable ΔE_γ was introduced, which was defined as:

$$\Delta E_\gamma = E'_\gamma - E''_\gamma, \quad (2)$$

where

$$E'_\gamma = \sqrt{s} - E_{\mu^+} - E_{\mu^-} \quad (3)$$

and

$$E''_\gamma = \frac{|\sin(\theta_{\mu^+} + \theta_{\mu^-})|}{|\sin(\theta_{\mu^+} + \theta_{\mu^-})| + \sin\theta_{\mu^+} + \sin\theta_{\mu^-}} \sqrt{s}. \quad (4)$$

In these formulae, θ_{μ^+} and θ_{μ^-} are the polar angles, and E_{μ^+} and E_{μ^-} the energies of the muons; the variable E''_γ is an approximation to the energy of an ISR photon emitted in the direction of one of the beams. This variable is also effective in rejecting tau events [27] and only events with $\Delta E_\gamma < 25$ GeV were retained.

Because the selection efficiencies could not be estimated reliably at low polar angles, the cross-sections were determined with samples of events with the μ^- polar angle in the region $20^\circ \leq \theta_{\mu^-} \leq 160^\circ$. For the measurement of the forward-backward asymmetries however, the likelihood fit method is not affected by the selection efficiencies if these are forward-backward symmetric (see section 7.3). Therefore, for these measurements the μ^- polar angle region was extended to $11^\circ \leq \theta_{\mu^-} \leq 169^\circ$.

After this selection of dimuon events, data runs were rejected if the parts of the DELPHI detector used in the analysis were not fully operational. The total number of dimuons available for the asymmetry analysis in the 1995 data amounted to 29,104. The total number of dimuons selected for the cross-section analysis was 22,389. From the 220,000 simulated $\mu^+\mu^-$ events, 183,318 remained after the dimuon selection in the polar angle region $20^\circ \leq \theta_{\mu^-} \leq 160^\circ$. The tau background was estimated with the simulated $\tau^+\tau^-$ events to be 0.20%. The background from two-photon events was also estimated with simulated events, and found to be less than 0.1% for the channel $e^+e^- \rightarrow e^+e^-\mu^+\mu^-$. No simulated events for the channel $e^+e^- \rightarrow e^+e^-\tau^+\tau^-$, were found to satisfy the dimuon selection criteria. The cosmic ray background was estimated from the data, by relaxing

the definition of the interaction region [1] and counting the number of additional events accepted in the data sample. It was found to amount to 0.43%.

To extract the events with ISR from the dimuon sample the same procedure was used as for the analysis of the 1991-1994 data [27]. To ensure a high purity of the selected sample for all effective annihilation energies ($\sqrt{s'}$), the selection criteria were taken to be different in each $\sqrt{s'}$ interval. Two sets of selections were used depending on whether or not a photon was detected in the electromagnetic calorimeters close to one of the muons.

For the effective annihilation energy $\sqrt{s'}$, or equivalently the $\mu^+\mu^-$ invariant mass $M_{\mu\mu}$, the following expression was used:

$$\sqrt{s'} = M_{\mu\mu} = \sqrt{s - 2E''_{\gamma}\sqrt{s}}. \quad (5)$$

The justification for this procedure is explained in [31]. The analysis was restricted to the $\sqrt{s'}$ region between 20 and 87 GeV.

In the 1995 data sample, 100 ISR events were selected for the cross-section calculation, and 124 for the asymmetry and helicity cross-section ratio calculation. From the 183,318 simulated dimuons, 980 ISR events were selected for the cross-section calculations.

The efficiency of the selection procedure and the contamination by FSR events were studied with a sample of about 146,000 simulated radiative muon events generated by DYMU3 with $\mu\mu$ invariant mass $M_{\mu\mu} < 88$ GeV. The resulting efficiency and the purity with respect to FSR events are displayed as a function of $\sqrt{s'}$ in Figure 14. The purity of the sample is near 90% over the whole energy interval. In this Figure the values obtained in ref. [27] for the data taken between 1991 and 1994 are also shown. The purity of the 1995 sample is the same within uncertainties as the purity of the previous sample. The selection efficiency for the 1995 data is however lower than the efficiencies obtained for the 1991-1994 data.

The cosmic ray background was checked using the sample of ISR events selected for the cross-section calculation. No additional events were found when the cuts on the interaction region definition were relaxed.

The background from $e^+e^- \rightarrow \tau^+\tau^-$ events was estimated from the sample of simulated $\tau^+\tau^-$ events. No events were found to satisfy the ISR selection criteria.

The background from two-photon processes was estimated from simulated events. It was found that the channel $e^+e^- \rightarrow e^+e^-\mu^+\mu^-$ contributed a background of 4.7%, mainly concentrated at low values of $\sqrt{s'}$.

9.2 Cross-sections

For the calculation of the cross-sections the polar angle of the μ^- was required to be in the range $20^\circ \leq \theta_{\mu^-} \leq 160^\circ$. A total of 100 events was selected from the 1995 data, and 980 events from the simulated sample.

The ratio of the averages of the observed to the Standard Model Improved Born [32] cross-sections inside a given $\sqrt{s'}$ interval is given by

$$\frac{\langle \sigma_{IB}^{obs}(\sqrt{s'}) \rangle}{\langle \sigma_{IB}^{SM}(\sqrt{s'}) \rangle} = \frac{N_{obs}(\sqrt{s'}) \cdot N_{sim}^{norm}}{N_{sim}(\sqrt{s'}) \cdot N_{obs}^{norm}}, \quad (6)$$

where $\sqrt{s'}$ is the mean effective annihilation energy in the interval. The quantities $N_{obs}(\sqrt{s'})$ and $N_{sim}(\sqrt{s'})$ represent the numbers of ISR events reconstructed in a given $\sqrt{s'}$ interval in the data and in the simulated sample respectively. The quantities N_{obs}^{norm} and N_{sim}^{norm} represent the total number of dimuon events selected in the real and

simulated data samples. In each $\sqrt{s'}$ interval, the normalisation of the ISR sample to the full dimuon sample was calculated separately for the on-peak and off-peak data, after which the results were averaged. The number $N_{obs}(\sqrt{s'})$ was corrected for the two-photon background, and the number N_{obs}^{norm} was also corrected for the background arising from cosmic ray and tau events. The other backgrounds were too small to justify a correction. It was verified that the selection efficiency for ISR events was the same for the observed data and the simulation.

Table 16 shows the number of ISR events selected in the 1995 data and in the simulated samples, as well as the cross-section ratio calculated with formula (6) as a function of $\sqrt{s'}$, up to an energy of 87 GeV. In determining these values, only statistical uncertainties were taken into account. The main source of systematic uncertainties was the modelling of the muon momenta in the simulation. To reduce these effects to a negligible size, the muon momenta were smeared in the simulation to match the resolution observed in the data.

Figure 15 shows the ratios between the observed and theoretical Improved Born cross-sections as a function of the effective annihilation energy for the 1995 data. In this Figure the cross-section ratios obtained from the analysis of the 1992-1994 data are also shown. The cross-section ratios from the two samples agree well. Consequently a weighted average was made of the numbers obtained from the two samples. The result of this procedure is shown in Table 16.

The observed cross-sections were calculated by multiplying the cross-section ratios with the Improved Born cross-sections predicted by the SM. The theoretical Improved Born cross-sections, $\sigma_{IB}^{SM}(\sqrt{s'})$, were obtained from the DYMU3 program. The parameters used in this calculation were $M_Z = 91.25$ GeV/c², $\alpha_Z = 2.562$ GeV/c², and $\sin^2 \theta_W = 0.2296$, which were the default values used by DELPHI for the generation of $\mu^+ \mu^-$ events. The results are independent of these assumed parameters. The observed cross-sections are displayed in Figure 16, together with the cross-sections for the reaction $e^+ e^- \rightarrow \mu^+ \mu^-$ obtained near the Z^0 peak [1,2] and those obtained at PEP, PETRA, and TRISTAN [33]. The published values were corrected for initial state radiation to obtain Improved Born values.

9.3 Asymmetries and helicity cross-sections

For the estimation of the forward-backward asymmetries, the polar angle of the μ^- was required to be in the range $11^\circ \leq \theta_{\mu^-} \leq 169^\circ$. A total of 124 events was selected from the 1995 data. The distribution of these events as a function of $\sqrt{s'}$ is shown in Table 17.

For events which are not produced in the $e^+ e^-$ c.m. frame, the angle between the μ^- and the e^- beam direction in the $\mu^- \mu^+$ rest frame is given by [34]:

$$\cos \theta^* = \frac{\sin \frac{1}{2}(\theta_{\mu^+} - \theta_{\mu^-})}{\sin \frac{1}{2}(\theta_{\mu^+} + \theta_{\mu^-})}, \quad (7)$$

where θ_{μ^+} and θ_{μ^-} are the polar angles of the μ^+ and the μ^- with respect to the e^- beam axis in the laboratory frame.

In each $\sqrt{s'}$ interval the $\cos \theta^*$ distribution for the 1995 data was compared to the distribution obtained for the 1991-94 data and was found to be the same within uncertainties. It was checked that the contamination of the 1995 sample by FSR events was the same as that found for the 1991-94 sample. Therefore the $\cos \theta^*$ distributions from

the 1991-94 sample could be added to that obtained from the 1995 sample. In total there were 523 events.

In each $\sqrt{s'}$ interval, the asymmetry A_{FB} was then obtained by performing a maximum likelihood fit of the raw $\cos \theta^*$ distribution to an expression of the form

$$\frac{dN}{d \cos \theta^*} = C [P_{isr}(1 + \cos^2 \theta^* + \frac{8}{3} A_{FB} \cos \theta^*) + P_{fsr}(1 + \cos^2 \theta^*) + P_{\gamma\gamma}(1 + \cos^2 \theta^* + \frac{8}{3} A_{FB}^{\gamma\gamma} \cos \theta^*)], \quad (8)$$

where the term P_{isr} represents the purity of the sample, which on average amounts to 90%, P_{fsr} and $P_{\gamma\gamma}$ are the contamination by FSR and $\gamma\gamma$ events and $A_{FB}^{\gamma\gamma}$ is the asymmetry for these $\gamma\gamma$ events (see Table 17). For the FSR events the asymmetry is taken to be zero, since this refers to the Z^0 peak. Formula (8) does not include radiative corrections. Since the asymmetries determined in this analysis are Improved Born asymmetries, and ISR is explicitly allowed for, only the electro-weak corrections should be considered. These are small compared to the experimental precision and modify the asymmetry by at most 0.02 in the energy region between 40 and 88 GeV. It was checked on simulated events that the selection efficiency for each $\cos \theta^*$ bin was compatible with that of the corresponding $-\cos \theta^*$ bin.

These fitted asymmetries are shown in Table 17, and are displayed in Figure 17 together with the SM prediction for the Improved Born asymmetry. Figure 17 also shows the asymmetries measured by DELPHI near the Z^0 peak (see [1,2]), after correction to Improved Born values. The SM Improved Born asymmetry was calculated with the DYMU3 program with the parameters mentioned in Section 9.2. The only source of systematic uncertainty on the asymmetry, $\delta(A_{FB})_{sys}^{fit}$, which was considered was that resulting from the uncertainty on the purity. The values of this uncertainty are shown in Table 17.

The helicity cross-sections $\tilde{\sigma}_+^\mu$ and $\tilde{\sigma}_-^\mu$ and their ratio (see [29]) were determined as follows. The raw $\cos \theta^*$ distribution in each $\sqrt{s'}$ interval was corrected for selection inefficiencies in the same way as described in [27]. This procedure relies on the fact that the distribution in $|\cos \theta^*|$ is symmetric and of the form $1 + \cos^2 \theta^*$. The $\cos \theta^*$ distributions were then corrected for the contamination by FSR and $\gamma\gamma$ events by subtracting a distribution obtained from simulated events. Next, in each bin of the $\cos \theta^*$ distribution the corrected content was multiplied by a weight factor:

$$F_\pm = A (1 \pm B \cos \theta^*), \quad (9)$$

where

$$A = \frac{2}{C_M(3 + C_M^2)}, \quad B = \frac{3 + C_M^2}{2C_M^2} \quad (10)$$

and $C_M = \cos \theta_{max}^*$, where θ_{max}^* defines the angular range studied. These weighted contents were summed for all $\cos \theta^*$ bins between -0.8 and $+0.8$ for $\sqrt{s'}$ below 65 GeV, and between -0.9 and $+0.9$ for the other $\sqrt{s'}$ values. The C_M limits were chosen depending on the statistics in each $\sqrt{s'}$ interval. The values of and statistical uncertainties on $\tilde{\sigma}_+^\mu$ and $\tilde{\sigma}_-^\mu$ were derived from the weighted sums. The uncertainty on the purity of the sample was taken into account in the systematic uncertainty. The numbers obtained are given as a function of $\sqrt{s'}$ in Table 17, together with the predictions of the Standard Model. The present measurements are in agreement with these predictions.

10 Fits to the Data

Fits to the data on the hadronic and leptonic cross-sections and the leptonic forward-backward asymmetries reported here, and to all the previously published DELPHI data [1,2] have been made. Full account was taken of the LEP energy uncertainties and their point-to-point and year-to-year correlations [5]. Allowance was also made for the correlations from year to year of the systematic uncertainties in the measured cross-sections and asymmetries.

10.1 Model-Independent Fits

Before QED radiative corrections, it is possible to write the cross-section for $e^+e^- \rightarrow \text{hadrons}$, $\sigma(s)$, in an almost model-independent form as

$$\sigma(s) = \sigma_0 \frac{s, \frac{2}{Z}}{(s - M_Z^2)^2 + (s^2/M_Z^2), \frac{2}{Z}},$$

where M_Z and $, \frac{2}{Z}$ are the Z^0 mass and width respectively and σ_0 can be expressed in terms of the hadronic and electronic partial widths, $, \text{had}$ and $, e$, as

$$\sigma_0 = \frac{12\pi, e, \text{had}}{M_Z^2, \frac{2}{Z}}.$$

The leptonic partial widths, $, f$, can be written in terms of effective vector and axial-vector coupling constants, g_{V_f} and g_{A_f} , as

$$, f = \frac{G_F M_Z^3}{6\pi\sqrt{2}} (g_{V_f}^2 + g_{A_f}^2) (1 + \delta_f^{QED}),$$

where $\delta_f^{(QED)}$ accounts for final state photonic corrections.

In order to fit the hadronic and leptonic cross-sections and the leptonic forward-backward asymmetries, the parameters M_Z , $, \frac{2}{Z}$, σ_0 , R_f and A_{FB}^{0f} were chosen. The parameters R_f and A_{FB}^{0f} are defined as

$$R_f = \frac{, \text{had}}{, f}$$

and

$$A_{\text{FB}}^{0f} = 3 \frac{g_{V_e} g_{A_e}}{(g_{V_e}^2 + g_{A_e}^2)} \frac{g_{V_f} g_{A_f}}{(g_{V_f}^2 + g_{A_f}^2)}.$$

This set of parameters was chosen because they have small correlations between them and are therefore preferred for combining results from the different LEP experiments. To lowest order the forward-backward asymmetry in the reaction $e^+e^- \rightarrow f^+f^-$ at $\sqrt{s} = M_Z$ is given by A_{FB}^{0f} and its variation away from the peak is mainly proportional to $g_{A_e} g_{A_f}$.

For the purpose of future comparisons and averaging of the lineshape results of the LEP experiments, an estimate of the uncertainties of the fitted parameters due to several common sources of uncertainty was obtained.

The LEP energy uncertainty represents one of the most important sources of uncertainty common to the different LEP experiments. An estimate of the LEP energy related contribution to the fitted parameter uncertainties was performed by comparing fit results with the nominal LEP energy uncertainties, with fit results obtained with these

uncertainties scaled by 5%. The LEP energy related uncertainties on M_Z and σ_Z are 1.6 MeV and 1.2 MeV respectively, which represent a considerable proportion of the total uncertainties. The significant uncertainties on the fitted parameters which are due to the LEP energy uncertainty are given in Tables 18 and 19. The uncertainties on R_e and its correlations also include the effect of the energy and M_Z dependence of the s-t interference contribution, which was subtracted to get the s-channel only numbers for the e^+e^- channel. As a cross-check of the energy calibration, the Z boson mass was determined independently for three different LEP calibration periods, namely 1990-1992, 1993-1994 and 1995. Technically this was done in a special fit with additional M_Z parameters M_Z^{90-92} , M_Z^{93-94} and M_Z^{95} . The results were $M_Z^{90-92} = 91.1883 \pm 0.0084$ GeV, $M_Z^{93-94} = 91.1824 \pm 0.0043$ GeV and $M_Z^{95} = 91.1894 \pm 0.0038$ GeV. All the fitted masses are consistent with each other within the uncertainties.

The computation of the luminosity in each LEP experiment relies on the theoretical prediction of the low angle Bhabha scattering cross-section. For the conditions of the DELPHI STIC determination, the uncertainty due to missing higher order terms is estimated [15] to be $\pm 0.06\%$, which can be considered as common to the other LEP experiments. This uncertainty translates into an uncertainty of ± 25 pb on σ_0 , the hadronic pole cross-section.

Relatively poor theoretical knowledge also influences the wide angle e^+e^- channel measurements through the procedure of the t-channel subtraction, which is performed in order to get the s-channel only numbers suitable for the fits. According to reference [23] theoretical uncertainties of 1.1 pb on the forward and 0.3 pb on the backward cross-sections may be assumed. The correlations between the uncertainties on the forward and backward cross-sections, and between the above and below peak energy points were varied between +1 and -1 in order to estimate the uncertainties in R_e and A_{FB}^0 due to this source. The estimates shown in Table 20 were obtained.

The program ZFITTER [22] was used to determine the parameters from fits to the experimental data. The theoretical formalism of ZFITTER takes account of the most up-to-date knowledge of initial and final state QED effects. According to the recommendation of the LEP Electroweak Working Group, A_{FB}^{0f} is defined in terms of the real parts of the couplings, whereas the leptonic partial widths are defined in terms of their magnitudes. The differences are insignificant with present experimental uncertainties, but are in any case correctly taken into account in the fits. Corrections arising from γ exchange and hadronic γ -Z interference are calculated within the framework of the Standard Model.

The uncertainties in the theoretical calculation used to extract the fit parameters have been discussed in a recent report [35]. Uncertainties which are relevant to the fit procedure applied in this paper arise from QED and electroweak corrections and from residual dependences of the Model Independent fits on Standard Model parameters. An estimation of the theoretical uncertainties was performed by comparing the TOPAZ0 [20] and ZFITTER [22] calculations with different input Standard Model parameters and program options. Uncertainties of 0.3 MeV and 0.2 MeV were found on M_Z and σ_Z respectively, with the main contribution coming from the QED effect of initial state pair production.

Carrying out a 9-parameter fit, allowing independent couplings for the three lepton species, the parameters shown in Table 21 were obtained. The χ^2/DF of this fit was 177/168. The correlation coefficients for the parameters of this fit are given in Table 22. The uncertainty on σ_Z includes a contribution of ± 0.2 MeV, common to all LEP experiments, due to the uncertainty of ± 1 MeV on the LEP centre-of-mass energy spread.

The fits reported here were made with a LEP energy error matrix specific to DELPHI. However it was checked that using an average LEP energy error matrix, appropriate for combining all LEP experiments results, the changes in the fitted parameters were insignificant.

Since the parameters are in good agreement with lepton universality, a 5-parameter fit assuming flavour independence of the couplings was performed. The resulting parameters are also given in Table 21. The χ^2/DF of this fit was 183/172. The correlation coefficients of the parameters of this fit are given in Table 23. Here R_l is defined for the Z^0 decay into a pair of massless charged leptons and is treated consistently throughout. The results of the 9-parameter and 5-parameter fits are in good agreement with those published by the other LEP collaborations [36–38].

In Figure 18 the result of the 5-parameter fit is shown together with the DELPHI data on the hadronic cross-sections. In Figure 19 and Figure 20 respectively are shown the DELPHI data on leptonic cross-sections and forward-backward asymmetries, compared to the results of the 5-parameter fit. All the leptonic data shown are corrected for the acollinearity and momentum cuts and extrapolated to the full solid angle where necessary.

From the results of the preceding fits the following parameters can be derived:

$$\begin{aligned} \sigma_{e} &= 83.54 \pm 0.27 \text{ MeV} \\ \sigma_{\mu} &= 84.48 \pm 0.40 \text{ MeV} \\ \sigma_{\tau} &= 83.71 \pm 0.58 \text{ MeV} \end{aligned}$$

from the 9-parameter fits and

$$\begin{aligned} \sigma_l &= 83.85 \pm 0.17 \text{ MeV} \\ \sigma_{\text{inv}} &= 498.1 \pm 3.2 \text{ MeV} \\ \sigma_{\text{had}} &= 1.7381 \pm 0.0040 \text{ GeV}. \end{aligned}$$

from the 5-parameter fits, where σ_{inv} is the partial width for decay into invisible particles.

11 Interpretation of the Results

Assuming the Minimal Standard Model value for $\sigma_{\nu/l}$:

$$\sigma_{\nu/l} = 1.991 \pm 0.001$$

(where the central value is evaluated for $M_Z = 91.1867 \text{ GeV}$, $m_t = 174.1 \text{ GeV}$ [39,40], $m_H = 150 \text{ GeV}$ and the uncertainty quoted accounts for a variation of m_t in the range $m_t = 174.1 \pm 5.4 \text{ GeV}$ and a variation of m_H in the range $90 < m_H(\text{GeV}) < 300$), and using our result:

$$\sigma_{\text{inv}/l} = 5.941 \pm 0.033$$

the number of light neutrino species can be deduced. The result is:

$$N_{\nu} = 2.984 \pm 0.017.$$

Within the context of the Minimal Standard Model, a fit has been made to the DELPHI data, leaving the values of the top mass m_t and the strong coupling constant $\alpha_s(M_Z^2)$ as free parameters. The results are:

$$\begin{aligned} m_t &= 178_{-15}^{+16+8} \text{ GeV} \\ \alpha_s(M_Z^2) &= 0.109 \pm 0.006 \pm 0.001. \end{aligned}$$

The central values were obtained assuming a Higgs boson mass m_H of 150 GeV, and the second uncertainty corresponds to the variation of m_H in the range $90 < m_H(\text{GeV}) < 300$. For the QED coupling constant, the hadronic contribution $\Delta\alpha_{\text{had}}^{(5)}(M_Z^2) = 0.02804 \pm 0.00065$ was taken from [41], and the leptonic contribution was accounted for in the ZFITTER program up to third order according to [42]. The value of m_t is consistent with direct measurements [39,40], and the value of $\alpha_s(M_Z^2)$ is in agreement with other determinations [43].

The partial widths for the Z decay into leptons, and the lepton forward-backward asymmetries can be combined to determine the magnitudes of the effective vector and axial-vector couplings. As defined above the asymmetries depend upon the ratio g_{V_l}/g_{A_l} whereas the leptonic partial widths depend upon $(g_{V_l}^2 + g_{A_l}^2)$. The following values are obtained:

$$\begin{aligned} g_{V_l}^2 &= (1.58 \pm 0.16) \times 10^{-3} \\ g_{A_l}^2 &= 0.2507 \pm 0.0005. \end{aligned}$$

The leptonic vector and axial-vector couplings correspond to a value of the weak mixing angle of

$$\sin^2 \theta_{eff}^{lept} = 0.2302 \pm 0.0010.$$

It is of interest to consider to what extent the measured values of the total and partial widths allow for the possibility of decays of the Z^0 into yet unknown particles. If such particles are “invisible” this can be deduced in a straightforward manner from the comparison of the measured value of Γ_{inv} to its Standard Model prediction. Whether the new particles are visible or invisible, they will contribute to the measured value of Γ_Z . Confronting the measured values of Γ_{inv} and Γ_Z with their Standard Model predictions allows a derivation of upper limits on the extra partial widths ($\Gamma_{\text{inv}}^{\text{new}}$ and Γ_Z^{new}) related to new physics. The Standard Model predictions were computed for $m_t = 174.1 \pm 5.4$ GeV [39,40], $\alpha_s(M_Z^2) = 0.118 \pm 0.003$ [43], $\alpha(M_Z^2)^{-1} = 128.896 \pm 0.090$ [41] and $M_H = 150_{-60}^{+150}$ GeV. The following values were obtained:

$$\begin{aligned} \Gamma_{\text{inv}}^{\text{new}} &= -3.5 \pm 3.2 \text{ MeV} \\ \Gamma_Z^{\text{new}} &= -6.7_{-5.1}^{+4.8} \text{ MeV}, \end{aligned}$$

leading to the following 95% confidence level limits, if $\Gamma_{\text{inv}}^{\text{new}}$ and Γ_Z^{new} are allowed only positive values:

$$\begin{aligned} \Gamma_{\text{inv}}^{\text{new}} &< 4.4 \text{ MeV} \\ \Gamma_Z^{\text{new}} &< 6.0 \text{ MeV}. \end{aligned}$$

The above limits assume that the Standard Model predictions for loop corrections are valid. However virtual effects from new physics could make this assumption unreliable. It has been suggested in ref. [44], that one can base an almost model-independent estimate of the partial width, Γ^{new} , for decays into unknown particles on the assumption that the cross-section and asymmetry measurements in the e^+e^- and $\mu^+\mu^-$ channels are reliable, that is these modes are unlikely to be contaminated by decays involving new particles. The analysis is done within the formalism of [45], so that no specific assumptions are made about loop corrections. The value of m_t is needed to evaluate the $b\bar{b}$ vertex, with the other vertex corrections assumed to behave normally.

Using the results of Section 10.1, we obtain for Γ^{new} and δ_{had} (the part of Γ^{new} leading to visible decays into hadronic final states):

$$\begin{aligned}\Gamma^{\text{new}} &= -5.3 \pm 4.8 \text{ MeV} \\ \delta_{\text{had}} &= -3.0 \pm 6.2 \text{ MeV}.\end{aligned}$$

If only positive values of Γ^{new} are allowed, a limit $\Gamma^{\text{new}} < 6.6 \text{ MeV}$ is obtained at the 95% confidence level.

12 Summary

DELPHI data from the LEP energy scans of 1993 and 1995 with precise monitoring of the beam energies, and those from a high statistics run in 1994 have been analysed in conjunction with data from previous years. The parameters of the Z^0 resonance have been determined with significantly improved precision compared to previous DELPHI publications. The analysis of $\mu^+\mu^-$ events with hard initial state photon observed in 1995 has been presented. When combined with published DELPHI measurements from data of previous years, results on the cross-sections and forward backward asymmetries for \sqrt{s} in the range 20-87 GeV have been obtained. All observations are consistent with the expectations of the Standard Model.

Acknowledgements

We thank the SL Division of CERN for the excellent performance of the LEP collider. The careful work of the Polarization group and the Working Group on LEP energy has been essential for the data presented here. We thank G. Passarino for helpful discussions. We are also grateful to the technical and engineering staffs in our laboratories and we acknowledge the support of
Austrian Federal Ministry of Science, Research and Arts,
FNRS-FWO, Belgium,
FINEP, CNPq, CAPES, FUJB and FAPERJ, Brazil,
Czech Ministry of Industry and Trade, GA CR 202/96/0450 and GA AVCR A1010521,
Danish Natural Research Council,
Commission of the European Communities (DG XII),
Direction des Sciences de la Matière, CEA, France,
Bundesministerium für Bildung, Wissenschaft, Forschung und Technologie, Germany,
General Secretariat for Research and Technology, Greece,
National Science Foundation (NWO) and Foundation for Research on Matter (FOM),
The Netherlands,
Norwegian Research Council,

State Committee for Scientific Research, Poland, 2P03B00108, 2P03B03311 and 628/E-78-SPUB-P03-023/97,
 JNICT–Junta Nacional de Investigação Científica e Tecnológica, Portugal,
 Vedecka grantova agentura MS SR, Slovakia, Nr. 95/5195/134,
 Ministry of Science and Technology of the Republic of Slovenia,
 CICYT, Spain, AEN96-1661 and AEN96-1681,
 The Swedish Natural Science Research Council,
 Particle Physics and Astronomy Research Council, UK,
 Department of Energy, USA, DE-FG02-94ER40817.

References

- [1] DELPHI Collaboration, P. Abreu et al., Nucl. Phys. **B417** (1994) 3.
- [2] DELPHI Collaboration, P. Abreu et al., Nucl. Phys. **B418** (1994) 403.
- [3] L. Arnaudon et al., Z.Phys. **C66** (1995) 45.
- [4] The LEP Energy Working Group, R. Assmann et al., Z. Phys. **C66** (1995) 567.
- [5] The LEP Energy Working Group, R. Assmann et al., Eur. J. Phys **C6** (1999) 187.
- [6] L. Arnaudon et al., Phys.Lett.B307 (1993),187
- [7] DELPHI Collaboration, P. Aarnio et al. , Nucl. Instr. & Meth. **A303** (1991) 233.
- [8] DELPHI Collaboration, P. Abreu et al. , Nucl. Instr. & Meth. **A378** (1996) 57.
- [9] S. Jadach et al., Phys. Lett. **B353** (1995) 362;
 S. Jadach, W. Placzek and B.F.L. Ward, Phys. Lett. **B353** (1995) 349.
- [10] R. Brun et al., “GEANT3”, CERN report DD/EE/84-1 (1987), CERN Program Library Long Writeup W5013.
- [11] F.A. Berends and R. Kleiss, Nucl. Phys. **B186** (1981) 22.
- [12] F.A. Berends, W. Hollik and R.Kleiss, Nucl. Phys. **B304** (1988) 712.
- [13] S. Jadach et al., Comp. Phys. Comm. **102** (1997) 229.
- [14] A.C.Benvenuti et al., “The DELPHI Small Angle Tile Calorimeter”, contribution to IEEE NSS 1994, and references therein.
- [15] S. Jadach et al., Phys. Lett. **B450** (1999) 262.
- [16] T. Sjöstrand, Comp. Phys. Comm. **39** (1986) 347;
 M. Bengtsson and T. Sjöstrand, Comp. Phys. Comm. **43** (1987) 367;
 T. Sjöstrand, Comp. Phys. Comm. **82** (1994) 74.
- [17] DELPHI Collaboration, P. Abreu at al., Z. Phys. **C73** (1996) 11.
- [18] S. Jadach, B.F.L. Ward and Z. Was, Comp. Phys. Comm. **66** (1991) 276.
- [19] S. Nova, A. Olchevski and T. Todorov, “Monte Carlo event generator for two photon processes”, DELPHI Note 90-35 (1990) (unpublished).
- [20] G. Montagna et al., Nucl. Phys. **B401** (1993) 3, and Comput. Phys. Commun. **76** (1993) 328.
- [21] W.J.P. Beenakker, F.A. Berends and S.C. van der Marck, Nucl. Phys. **B349** (1991) 323.
- [22] D. Bardin et al., “ZFITTER V.6.21: A Semi-analytical Program for Fermion Pair Production in e^+e^- Annihilation”, preprint DESY-99-070 (1999). hep-ph/9908433.
- [23] W. Beenaker and G. Passarino, Phys. Lett. **B425** (1998) 199, and private communication.
- [24] J.E. Campagne and R. Zitoun, Z. Phys **C43** (1989) 469 and Proc. Radiative Corrections–Results and Perspectives, Brighton, 9–14 July 1989, p271.

- [25] F.A. Berends, P.H. Daverveldt and R. Kleiss, *Comp. Phys. Comm.* **40** (1986) 271, 285, 309.
- [26] S. Jadach et al., *Phys. Lett.* **B390** (1997) 298.
- [27] DELPHI Collaboration, P. Abreu et al., *Z. Phys.* **C75** (1997) 581.
- [28] ALEPH Collaboration, R. Barate et al., *Phys. Lett.* **B399** (1997) 329;
L3 Collaboration, M. Acciari et al., *Phys. Lett.* **B374** (1996) 331;
OPAL Collaboration, P.D. Acton et al., *Phys. Lett.* **B273** (1991) 338.
- [29] J.-M. Frère, V.A. Novikov, M.I. Vysotsky, *Phys. Lett.* **B386** (1996) 437.
- [30] J. Hilgart, R. Kleis, *Comp. Phys. Comm.* **75** (1993) 191.
- [31] DELPHI Collaboration, P. Abreu et al., *Z. Phys.* **C65** (1995) 603.
- [32] F. Berends, “Z lineshape”, *Z Physics at LEP I*, CERN 89-08, Volume 1 (1989).
- [33] HRS Collaboration, M. Derrick et al., *Phys. Rev.* **D31** (1985) 2352;
MAC Collaboration, W. W. Ash et al., *Phys. Rev. Lett.* **55** (1985) 1831;
TASSO Collaboration, W. Braunschweig et al., *Z. Phys.* **C40** (1988) 163;
CELLO Collaboration, H.-J. Behrend et al., *Phys. Lett.* **B191** (1987) 209;
JADE Collaboration, W. Bartel et al., *Z. Phys.* **C26** (1985) 507;
MARK J Collaboration, B. Adeva et al., *Phys. Rev.* **D38** (1988) 2665;
AMY Collaboration, A. Bacala et al., *Phys. Lett.* **B218** (1989) 112;
AMY Collaboration, C. Velissaris et al., *Phys. Lett.* **B331** (1994) 227;
TOPAZ Collaboration, B. Howell et al., *Phys. Lett.* **B291** (1992) 206;
VENUS: K. Miyabayashi, *Recent electroweak results from TRISTAN*, Proc. of the XXXth Rencontres de Moriond, Les Arcs, March 1995, ed. J. Trân Thanh Vân.
- [34] Z. Was and S. Jadach, *Phys. Rev.* **D41** (1990) 1425.
- [35] D. Bardin, G. Passarino and M. Grünewald, Precision Calculation Project Report, hep-9902452.
- [36] ALEPH Collaboration, D. Buskulic et al., *Z. Phys.* **C62** (1994) 539;
ALEPH Collaboration, R. Barate et al., “Measurement of the Z Resonance Parameters at LEP”, preprint CERN-EP/99-104(1999), submitted to *Eur. J. Phys. C*.
- [37] L3 Collaboration, M. Acciarri et al., *Z. Phys* **C62** (1994) 551.
- [38] OPAL Collaboration, R. Akers et al., *Z. Phys.* **C61** (1994) 19.
- [39] CDF Collaboration, W. Yao et al., “Top Quark Mass from CDF”, Proc. 28th Int. Conf. on High Energy Physics, Vancouver, July 1998, p1093.
- [40] D0 Collaboration, B. Abbott et al., *Phys. Rev.* **D58** (1998) 052001.
- [41] S. Eidelmann and F. Jegerlehner, *Z. Phys.* **C67** (1995) 585.
- [42] M. Steinhauser, *Phys. Lett.* **B429** (1998) 158.
- [43] R.M. Barnett et al., *Eur. J. Phys.* **C3** (1998) 1.
- [44] K. Mönig, “Model Independent Limit of the Z-Decay-Width into Unknown Particles”, preprint CERN/OPEN-97-040 (1997).
- [45] G. Altarelli, R. Barbieri and F. Caravaglios, *Nucl. Phys.* **B349** (1995) 145.

Year	Peak-2	cal. fills	Peak	cal. fills	Peak+2	cal. fills
1993	10 pb ⁻¹	13/38(35%)	20 pb ⁻¹	1/57(2%)	10 pb ⁻¹	11/31(45%)
1994			60 pb ⁻¹	11/167(8%)		
1995	10 pb ⁻¹	14/22(69%)	20 pb ⁻¹	1/14(6%)	10 pb ⁻¹	13/23(65%)

Table 1: Luminosities and calibration runs per year and per energy point for the data collected in 1993-1995. The integrated luminosities are approximate, since the analyses of different channels required different selections of runs. The two values in the calibrated fills columns express the number of fills with at least one successful calibration divided by the total number of fills and the other shows the percentage of calibrated integrated luminosity.

Source of systematics	Contribution to $\frac{\Delta\mathcal{L}}{\mathcal{L}}$ (%)
Ring mask radius	± 0.02
ϕ mask acceptance	± 0.03
Unmasked acceptance borders	± 0.14
Interaction point $\langle z \rangle$	± 0.10
Interaction point $\langle x, y \rangle$ plus tilt	± 0.05
Energy cut	± 0.10
Data behind ϕ -mask	± 0.11
Less than 65% of energy in inner ring	± 0.01
Trigger efficiency	± 0.01
Off-momentum background	± 0.01
Monte Carlo statistics	± 0.04
Total experimental	± 0.24
Total theoretical	± 0.17
Total systematic uncertainty	± 0.29

Table 2: Contributions to the systematic uncertainty on the SAT absolute luminosity measurement.

Source of systematics	Contribution to $\frac{\Delta\mathcal{L}}{\mathcal{L}}$ (%)
uncert. in correction factors (uncorrelated part)	± 0.020
cut at the outer ring	± 0.015
cut at the inner edge	± 0.020
uncert. in measured parameters	± 0.015
energy cut	± 0.015
trigger efficiency and Bhabha selection	± 0.010
statistical uncertainty	± 0.050

Table 3: Contributions to the uncertainty of the VSAT luminosity measurement at the “peak+2” point.

Source of systematics	Contribution to $\frac{\Delta\mathcal{L}}{\mathcal{L}}$ (%)
IP position	± 0.06
Mask technique	± 0.04
MC statistics	± 0.03
R_A^{in} cut	± 0.02
R_A^{out} cut	± 0.02
Acoplanarity cut	± 0.01
Energy cut	± 0.03
Background subtraction	± 0.02
Trigger inefficiency	± 0.02
Total experimental	± 0.09
Total theoretical	± 0.06

Table 4: Contributions to the systematic uncertainty of the STIC luminosity measurement.

year	Collision energy (GeV)	Detector instabilities (%)	Forward inefficiencies (%)
1993	89.431	-0.010 ± 0.005	-0.16 ± 0.05
	91.187	-0.010 ± 0.005	-0.16 ± 0.05
	91.303	-0.11 ± 0.02	-0.16 ± 0.05
	93.015	-0.010 ± 0.005	-0.16 ± 0.05
1994	91.200	-0.040 ± 0.010	-0.18 ± 0.07
	91.204	-0.019 ± 0.010	-0.18 ± 0.07
1995	89.438	-0.005 ± 0.002	-0.10 ± 0.04
	91.278	-0.003 ± 0.002	-0.10 ± 0.04
	91.292	-0.006 ± 0.002	-0.10 ± 0.04
	92.965	-0.004 ± 0.002	-0.10 ± 0.04

Table 5: Corrections to the selection efficiencies for hadronic events due to detector instabilities and to detection and track reconstruction inefficiencies in the forward region not included in the Monte Carlo simulation. The uncertainties quoted are systematic.

Collision energy (GeV)	89.438	91.278	91.292	92.965
Monte Carlo statistics	± 0.02	± 0.02	± 0.02	± 0.02
forward inefficiency	± 0.04	± 0.04	± 0.04	± 0.04
off-peak efficiency correction	± 0.02	-	-	± 0.02
cut variations	± 0.08	± 0.08	± 0.08	± 0.08
total uncertainty on sel. eff.	± 0.09	± 0.09	± 0.09	± 0.09
$\tau^+\tau^-$ background	± 0.03	± 0.03	± 0.03	± 0.03
e^+e^- background	± 0.02	± 0.01	± 0.01	± 0.01
$\gamma\gamma$ collision background	± 0.03	± 0.01	± 0.01	± 0.02
total uncertainty	± 0.10	± 0.10	± 0.10	± 0.10

Table 6: Breakdown of the systematic uncertainties (in per-cent) on the 1995 hadronic cross-sections related to the knowledge of the selection efficiency and of the residual backgrounds.

year	Collision energy (GeV)	Cross-section (nb)
1993	89.431	9.868 ± 0.035
	91.187	30.351 ± 0.060
	91.303*	30.424 ± 0.098
	93.015	13.893 ± 0.041
1994	91.200	30.466 ± 0.034
	91.204	30.417 ± 0.152
1995	89.438	9.930 ± 0.038
	91.279	30.631 ± 0.105
	91.292*	30.650 ± 0.075
	92.965	14.348 ± 0.045

Table 7: DELPHI hadronic cross-sections measured from 1993 to 1995. In this table and tables 8-10, data taken during the “pre-scan” operation are indicated with *. The uncertainties quoted are statistical. They do not include overall normalisation uncertainties coming from efficiencies and backgrounds ($\pm 0.10\%$ in 1993 and 1995, and $\pm 0.11\%$ in 1994) and from the absolute luminosity ($\pm 0.29\%$ in 1993 and $\pm 0.11\%$ in 1994 and 1995).

year	Collision energy (GeV)	Cross-section (nb)	A_{FB}^e
1993	89.430	0.299 ± 0.008	-0.129 ± 0.028
	91.186	0.902 ± 0.011	0.026 ± 0.012
	91.303*	0.916 ± 0.014	-0.020 ± 0.016
	93.014	0.397 ± 0.007	0.085 ± 0.017
1994	91.201	0.909 ± 0.005	-0.001 ± 0.006
1995	89.438	0.302 ± 0.009	-0.136 ± 0.030
	91.278	0.928 ± 0.017	0.009 ± 0.018
	91.292*	0.908 ± 0.012	0.000 ± 0.013
	92.965	0.433 ± 0.007	0.101 ± 0.017

Table 8: DELPHI cross-sections and forward-backward asymmetries measured in the e^+e^- channel. The results refer to the polar angle range $44^\circ < \theta < 136^\circ$. The cut on acollinearity given in the text applies to both sets of results which refer to the s-channel only. The uncertainties quoted are statistical. The systematic uncertainties are listed in Tables 11, 12 and 13.

year	Collision energy (GeV)	Cross-section (nb)	A_{FB}^μ
1993	89.431	0.427 ± 0.007	-0.141 ± 0.015
	91.187	1.324 ± 0.012	-0.007 ± 0.008
	91.302*	1.354 ± 0.017	0.016 ± 0.013
	93.015	0.617 ± 0.008	0.104 ± 0.012
1994	91.200	1.331 ± 0.006	0.007 ± 0.004
1995	89.438	0.436 ± 0.007	-0.154 ± 0.016
	91.279	1.359 ± 0.018	0.020 ± 0.012
	91.292*	1.351 ± 0.013	0.000 ± 0.008
	92.965	0.649 ± 0.009	0.086 ± 0.012

Table 9: DELPHI cross-sections and forward-backward asymmetries measured in the $\mu^+\mu^-$ channel. The cross-sections are for the polar angle range $20^\circ < \theta < 160^\circ$ and the asymmetries refer to the full solid angle. The cuts on momenta and acollinearity given in the text apply to both sets of results. The uncertainties quoted are statistical. The systematic uncertainties are listed in Tables 11, 12 and 13.

year	Collision energy (GeV)	Cross-section (nb)	A_{FB}^{τ}
1993	89.431	0.470 ± 0.009	-0.156 ± 0.020
	91.187	1.477 ± 0.015	-0.007 ± 0.011
	91.303*	1.502 ± 0.021	0.002 ± 0.017
	93.015	0.665 ± 0.011	0.110 ± 0.016
1994	91.200	1.479 ± 0.007	0.015 ± 0.005
1995	89.438	0.494 ± 0.010	-0.126 ± 0.019
	91.278	1.465 ± 0.023	-0.006 ± 0.015
	91.292*	1.461 ± 0.017	0.018 ± 0.011
	92.965	0.696 ± 0.011	0.121 ± 0.015

Table 10: DELPHI cross-sections and forward-backward asymmetries measured in the $\tau^+\tau^-$ channel. The cross-sections and asymmetries refer to the full solid angle and the cuts on momenta and acollinearity given in the text are corrected for. The uncertainties quoted are statistical. The systematic uncertainties are listed in Tables 11, 12 and 13.

	Hadrons	e^+e^-	$\mu^+\mu^-$	$\tau^+\tau^-$
Cross-section				
θ acceptance ($^\circ$)	0-180	44-136	20-160	20-160
Selected events	682,262	24,286	28,888	21,920
Selection efficiency (%)	94.84 ± 0.09	97.82 ± 0.07	93.89 ± 0.26	61.99 ± 0.36
Trigger efficiency (%)	> 99.99	> 99.99	99.88 ± 0.01	99.98 ± 0.01
$\tau^+\tau^-$ background (%)	0.38 ± 0.03	1.10 ± 0.04	1.10 ± 0.11	–
$q\bar{q}$ background (%)	–	–	–	0.84 ± 0.15
$e^+e^- + \mu^+\mu^-$ bkgd. (%)	0.04 ± 0.01	–	–	1.60 ± 0.17
Two-photon bkgd. (pb)	16 ± 3	–	–	$1.9 \pm 0.5^*$
Cosmic ray bkgd. (%)	–	–	0.11 ± 0.03	0.11 ± 0.05
Tot. syst. uncert. (%)	± 0.10	$\pm 0.46^\dagger$	± 0.28	± 0.60
Asymmetry A_{FB}^f				
θ acceptance ($^\circ$)	–	44-136	11-169	20-160
Selected events	–	24,286	27,492	16,091
Tot. syst. uncert.	–	$\pm 0.0026^\dagger$	± 0.0009	± 0.0020

Table 11: Summary of event samples, angular acceptances, efficiencies (within the acceptances for e^+e^- and $\mu^+\mu^-$), backgrounds and systematic uncertainties in the hadronic and leptonic cross-sections, and the leptonic forward-backward asymmetries for the 1993 data. The values refer to the Z^0 peak and may differ at other energies. The e^+e^- data refer specifically to analysis method 2. The total systematic uncertainty of $\pm 0.29\%$ in the luminosity is not included in the above numbers for the cross-sections.

[†] Includes the uncertainty due to the t-channel subtraction.

* Includes the relevant four-fermion final state background.

	Hadrons	e^+e^-	$\mu^+\mu^-$	$\tau^+\tau^-$
Cross-section				
θ acceptance ($^\circ$)	0-180	44-136	20-160	20-160
Selected events	1,310,243	41,290	56,856	38,317
Selection efficiency (%)	94.79 ± 0.10	96.95 ± 0.06	95.27 ± 0.25	63.79 ± 0.36
Trigger efficiency (%)	> 99.99	> 99.99	99.73 ± 0.01	99.98 ± 0.01
$\tau^+\tau^-$ background (%)	0.41 ± 0.03	0.83 ± 0.04	1.14 ± 0.06	–
$q\bar{q}$ background (%)	–	–	–	0.92 ± 0.10
$e^+e^- + \mu^+\mu^-$ bkgd. (%)	0.04 ± 0.01	–	–	2.07 ± 0.20
Two-photon bkgd. (pb)	16 ± 3	–	–	$1.9 \pm 0.2^*$
Cosmic ray bkgd. (%)	–	–	0.07 ± 0.02	0.11 ± 0.05
Tot. syst. uncert. (%)	± 0.11	$\pm 0.52^\dagger$	± 0.26	± 0.60
Asymmetry A_{FB}^f				
θ acceptance ($^\circ$)	–	44-136	11-169	20-160
Selected events	–	41,290	58,532	26,479
Tot. syst. uncert.	–	$\pm 0.0021^\dagger$	± 0.0005	± 0.0020

Table 12: Summary of event samples, angular acceptances, efficiencies (within the acceptances for e^+e^- and $\mu^+\mu^-$), backgrounds and systematic uncertainties in the hadronic and leptonic cross-sections, and the leptonic forward-backward asymmetries for the 1994 data. The e^+e^- data refer specifically to analysis method 2. The total systematic uncertainty of $\pm 0.14\%$ in the luminosity is not included in the above numbers for the cross-sections.

† Includes the uncertainty due to the t-channel subtraction.

$*$ Includes the relevant four-fermion final state background.

	Hadrons	e^+e^-	$\mu^+\mu^-$	$\tau^+\tau^-$
Cross-section				
θ acceptance ($^\circ$)	0-180	44-136	20-160	20-160
Selected events	659,331	20,833	26,211	18,787
Selection efficiency (%)	95.34 ± 0.09	97.42 ± 0.08	94.40 ± 0.26	62.00 ± 0.36
Trigger efficiency (%)	> 99.99	> 99.99	99.74 ± 0.01	99.98 ± 0.01
$\tau^+\tau^-$ background (%)	0.38 ± 0.03	0.85 ± 0.04	1.22 ± 0.10	–
$q\bar{q}$ background (%)	–	–	–	1.10 ± 0.15
$e^+e^- + \mu^+\mu^-$ bkgd. (%)	0.02 ± 0.01	–	–	1.49 ± 0.13
Two-photon bkgd. (pb)	16 ± 3	–	–	$2.64 \pm 0.32^*$
Cosmic ray bkgd. (%)	–	–	0.09 ± 0.03	0.02 ± 0.01
Tot. syst. uncert. (%)	± 0.10	$\pm 0.52^\dagger$	± 0.28	± 0.60
Asymmetry A_{FB}^f				
θ acceptance ($^\circ$)	–	44-136	11-169	20-160
Selected events	–	20,833	29,143	19,551
Tot. syst. uncert.	–	$\pm 0.0020^\dagger$	± 0.0011	± 0.0020

Table 13: Summary of event samples, angular acceptances, efficiencies (within the acceptances for e^+e^- and $\mu^+\mu^-$), backgrounds and systematic uncertainties in the hadronic and leptonic cross-sections, and the leptonic forward-backward asymmetries for the 1995 data. The values refer to the Z^0 peak and may differ at other energies. The e^+e^- data refer specifically to analysis method 2. The total systematic uncertainty of $\pm 0.14\%$ in the luminosity is not included in the above numbers.

[†] Includes the uncertainty due to the t-channel subtraction.

* Includes the relevant four-fermion final state background.

$q - \bar{q}$	Syst. Uncert. (%)	1990	1991	1992	1993	1994	1995
1990	± 0.40	1.00	0.28	0.12	0.16	0.16	0.16
1991	± 0.20	0.28	1.00	0.25	0.32	0.32	0.32
1992	± 0.13	0.12	0.25	1.00	0.49	0.49	0.49
1993	± 0.10	0.16	0.32	0.49	1.00	0.64	0.64
1994	± 0.10	0.16	0.32	0.49	0.64	1.00	0.64
1995	± 0.10	0.16	0.32	0.49	0.64	0.64	1.00
e^+e^-	Syst. Uncert. (%)	1990	1991	1992	1993	1994	1995
1990	± 0.80	1.00	0.63	0.36	0.40	0.40	0.40
1991	± 0.50	0.63	1.00	0.57	0.65	0.65	0.65
1992	± 0.59	0.36	0.57	1.00	0.55	0.55	0.55
1993	± 0.52	0.40	0.65	0.55	1.00	0.62	0.62
1994	± 0.52	0.40	0.65	0.55	0.62	1.00	0.62
1995	± 0.52	0.40	0.65	0.55	0.62	0.62	1.00
$\mu^+\mu^-$	Syst. Uncert. (%)	1990	1991	1992	1993	1994	1995
1990	± 0.80	1.00	0.63	0.50	0.16	0.18	0.17
1991	± 0.50	0.63	1.00	0.80	0.26	0.29	0.27
1992	± 0.40	0.50	0.80	1.00	0.32	0.36	0.33
1993	± 0.31	0.16	0.26	0.32	1.00	0.46	0.43
1994	± 0.28	0.18	0.29	0.36	0.46	1.00	0.48
1995	± 0.30	0.17	0.27	0.33	0.43	0.48	1.00
$\tau^+\tau^-$	Syst. Uncert. (%)	1990	1991	1992	1993	1994	1995
1990	± 1.20	1.00	0.63	0.31	0.31	0.31	0.31
1991	± 0.75	0.63	1.00	0.49	0.49	0.49	0.49
1992	± 0.60	0.31	0.49	1.00	0.61	0.61	0.61
1993	± 0.60	0.31	0.49	0.61	1.00	0.61	0.61
1994	± 0.60	0.31	0.49	0.61	0.61	1.00	0.61
1995	± 0.60	0.31	0.49	0.61	0.61	0.61	1.00

Table 14: The systematic uncertainties due to selection efficiencies and background subtractions and their correlation coefficients between years in the measurements of hadronic and leptonic cross-sections. All numbers refer to measurements at the Z^0 peak and, in the e^+e^- case, the uncertainties apply to the s-channel. The systematic uncertainties due to the luminosity determination are not included.

e^+e^-	Syst. Uncert.	1990	1991	1992	1993	1994	1995
1990	± 0.0030	1.00	0.67	0.44	0.34	0.41	0.41
1991	± 0.0020	0.67	1.00	0.67	0.51	0.61	0.61
1992	± 0.0030	0.44	0.67	1.00	0.34	0.41	0.41
1993	± 0.0025	0.34	0.51	0.34	1.00	0.49	0.49
1994	± 0.0021	0.41	0.61	0.41	0.49	1.00	0.58
1995	± 0.0021	0.41	0.61	0.41	0.49	0.58	1.00
$\mu^+\mu^-$	Syst. Uncert.	1990	1991	1992	1993	1994	1995
1990	± 0.0050	1.00	0.60	0.20	0.06	0.10	0.03
1991	± 0.0030	0.60	1.00	0.33	0.09	0.17	0.06
1992	± 0.0010	0.20	0.33	1.00	0.28	0.50	0.17
1993	± 0.0009	0.06	0.09	0.28	1.00	0.56	0.19
1994	± 0.0005	0.10	0.17	0.50	0.56	1.00	0.33
1995	± 0.0015	0.03	0.06	0.17	0.19	0.33	1.00
$\tau^+\tau^-$	Syst. Uncert.	1990	1991	1992	1993	1994	1995
1990	± 0.0050	1.00	0.40	0.12	0.23	0.23	0.23
1991	± 0.0020	0.40	1.00	0.29	0.56	0.56	0.56
1992	± 0.0017	0.12	0.29	1.00	0.66	0.66	0.66
1993	± 0.0020	0.23	0.56	0.66	1.00	0.56	0.56
1994	± 0.0020	0.23	0.56	0.66	0.56	1.00	0.56
1995	± 0.0020	0.23	0.56	0.66	0.56	0.56	1.00

Table 15: The systematic uncertainties in the measurements of leptonic forward-backward asymmetries and their correlation coefficients between years. All numbers refer to measurements at the Z^0 peak, and in the e^+e^- case the uncertainties apply to the s-channel.

$\sqrt{s'}$ [GeV]	24-38	38-45	45-52	52-59	59-66	66-73	73-80	80-84	84-87
N_{obs}^{95}	2	9	2	5	5	7	11	16	43
N_{sim}^{95}	14	44	27	47	33	45	108	193	466
$\langle \sigma_{IB}^{obs} \rangle / \langle \sigma_{IB}^{SM} \rangle$	0.92	1.56	0.59	1.04	0.83	1.15	0.95	0.82	0.97
1995	± 1.03	± 0.62	± 0.59	$\pm .59$	± 0.68	± 0.52	± 0.31	± 0.20	± 0.15
$\langle \sigma_{IB}^{obs} \rangle / \langle \sigma_{IB}^{SM} \rangle$	1.14	0.99	1.01	0.76	0.56	1.05	0.93	0.90	1.11
1992-1995	± 0.49	± 0.23	± 0.33	± 0.21	± 0.18	± 0.23	± 0.14	± 0.11	± 0.06
$\langle \sqrt{s'} \rangle$ [GeV]	33.6	41.7	47.5	55.6	62.1	70.2	77.4	82.5	85.8
σ_{IB}^{SM} [pb]	86.6	56.5	43.9	32.9	27.6	24.9	29.6	49.8	106.1
σ_{IB}^{obs} [pb](92-95)	98.7	55.9	44.3	25.0	15.5	26.1	27.5	44.8	117.8
$\delta(\sigma_{IB}^{obs})$ [pb](92-95)	± 42.4	± 13.0	± 14.5	± 6.9	± 5.0	± 5.7	± 4.1	± 5.5	± 6.4

Table 16: Numbers of ISR events found in the 1995 data (N_{obs}^{95}) and simulated samples (N_{sim}^{95}) for different $\sqrt{s'}$ intervals; rows 3 and 4 show the ratios of the average measured cross-sections to the Born cross-section calculation described in the text for 1995, and their uncertainties. Rows 5 and 6 give the cross-section ratio and uncertainty for the data taken in 1992 to 1995. Row 7 gives the mean measured effective annihilation energy $\langle \sqrt{s'} \rangle$ in the interval, and row 8 gives within each energy interval σ_{IB}^{SM} , the mean Improved Born cross-section expected in the Standard Model, obtained from the DYMU3 program. Rows 9 and 10 give the resulting measured cross-section σ_{IB}^{obs} with its uncertainty $\delta(\sigma_{IB}^{obs})$

$\sqrt{s'}$ [GeV]	20-50	50-65	65-80	80-84	84-87
N_F^{95}	9	6	4	4	17
N_B^{95}	6	8	19	17	34
$P_{\gamma\gamma}$	0.10	0.07	0.01	0.	0.
$A_{FB}^{\gamma\gamma}$ [%]	-49.	-24.	-75.		
$\langle \sqrt{s'} \rangle$ [GeV]	42.5	58.9	74.4	82.4	85.9
$A_{FB}^{fit} corr$ [%]	14.3 ± 14.4	-37.4 ± 15.6	-68.2 ± 7.0	-63.3 ± 8.4	-45.3 ± 6.2
$\delta(A_{FB})_{sys}^{fit}$ [%]	± 0.4	± 0.6	± 0.7	± 0.6	± 0.3
$\tilde{\sigma}_+^\mu / \tilde{\sigma}_-^\mu$	1.54 ± 0.55	0.34 ± 0.17	0.09 ± 0.05	0.10 ± 0.06	0.23 ± 0.05
δ_{sys}	0.05	0.01	0.01	0.01	0.01
$(\tilde{\sigma}_+^\mu / \tilde{\sigma}_-^\mu)^{SM}$	0.68	0.36	0.04	0.07	0.25

Table 17: N_F^{95}, N_B^{95} : observed number of ISR events in the forward and backward hemispheres for the 1995 data; $P_{\gamma\gamma}$: contamination by $\gamma\gamma$ events; $A_{FB}^{\gamma\gamma}$: asymmetry for $\gamma\gamma$ events as determined from simulated data; $\langle \sqrt{s'} \rangle$: the mean measured effective annihilation energy in the interval; $A_{FB}^{fit} corr$: the asymmetry with statistical uncertainty calculated with a maximum likelihood fit, corrected for FSR and $\gamma\gamma$ contamination, with systematic uncertainty $\delta(A_{FB})_{sys}^{fit}$, based on the data from 1991 to 1995; $\tilde{\sigma}_+^\mu / \tilde{\sigma}_-^\mu$: the helicity component ratio with its statistical uncertainty based on the data from 1991 to 1995; δ_{sys} : the systematic uncertainty on the above helicity component ratio; $(\tilde{\sigma}_+^\mu / \tilde{\sigma}_-^\mu)^{SM}$: SM prediction for the helicity component ratio.

	M_Z	\sqrt{s}, z	σ_0	R_e
M_Z	0.0016^2	–		
\sqrt{s}, z	$-(0.0005)^2$	0.0012^2	–	
σ_0	$-(0.0025)^2$	$-(0.0024)^2$	0.0093^2	–
R_e	0.0014^2	0.0000^2	0.0042^2	0.0159^2

Table 18: Covariance matrix of the uncertainties on the Model-Independent parameters, due to the uncertainties in the LEP energies.

	$A_{\text{FB}}^{0\ e}$	$A_{\text{FB}}^{0\ \mu}$	$A_{\text{FB}}^{0\ \tau}$
$A_{\text{FB}}^{0\ e}$	0.0004^2	–	
$A_{\text{FB}}^{0\ \mu}$	$-(0.0003)^2$	0.0003^2	–
$A_{\text{FB}}^{0\ \tau}$	$-(0.0003)^2$	0.0003^2	0.0003^2

Table 19: Covariance matrix of the uncertainties on the lepton forward asymmetries, due to the uncertainties in the LEP energies.

	R_e	$A_{\text{FB}}^{0\ e}$
R_e	0.025^2	–
$A_{\text{FB}}^{0\ e}$	$-(0.0058)^2$	0.0016^2

Table 20: Covariance matrix of the uncertainties on R_e and $A_{\text{FB}}^{0\ e}$, due to the theoretical uncertainties in the QED t-channel subtraction.

Parameter	Value (9-par)	Value (5-par)
M_Z (GeV)	91.1864 ± 0.0028	91.1863 ± 0.0028
\sqrt{s}, z (GeV)	2.4876 ± 0.0041	2.4876 ± 0.0041
σ_0 (nb)	41.578 ± 0.069	41.578 ± 0.069
R_e	20.88 ± 0.12	–
R_μ	20.65 ± 0.08	–
R_τ	20.84 ± 0.13	–
R_l	–	20.730 ± 0.060
$A_{\text{FB}}^{0\ e}$	0.0171 ± 0.0049	–
$A_{\text{FB}}^{0\ \mu}$	0.0165 ± 0.0025	–
$A_{\text{FB}}^{0\ \tau}$	0.0241 ± 0.0037	–
A_{FB}^0	–	0.0187 ± 0.0019

Table 21: The results of the 9-parameter and 5-parameter fits to all DELPHI data on hadronic and leptonic cross-sections and leptonic forward-backward asymmetries.

	, z	σ_0	R_e	R_μ	R_τ	$A_{\text{FB}}^{0\ e}$	$A_{\text{FB}}^{0\ \mu}$	$A_{\text{FB}}^{0\ \tau}$
M_Z	0.05	-0.07	0.06	0.00	0.00	0.06	0.06	0.04
, z	-	-0.27	0.00	-0.01	0.00	0.00	0.01	0.00
σ_0		-	0.12	0.19	0.11	-0.01	0.00	0.00
R_e			-	0.05	0.03	-0.11	0.03	0.02
R_μ				-	0.05	0.00	0.01	0.00
R_τ					-	0.00	0.00	0.01
$A_{\text{FB}}^{0\ e}$						-	-0.02	-0.02
$A_{\text{FB}}^{0\ \mu}$							-	0.01

Table 22: The correlation coefficients for the parameters of the 9-parameter fit.

	, z	σ_0	R_l	A_{FB}^0
M_Z	0.05	-0.07	0.03	0.10
, z	-	-0.27	-0.01	0.01
σ_0		-	0.24	-0.01
R_l			-	0.00

Table 23: The correlation coefficients for the parameters of the 5-parameter fit.

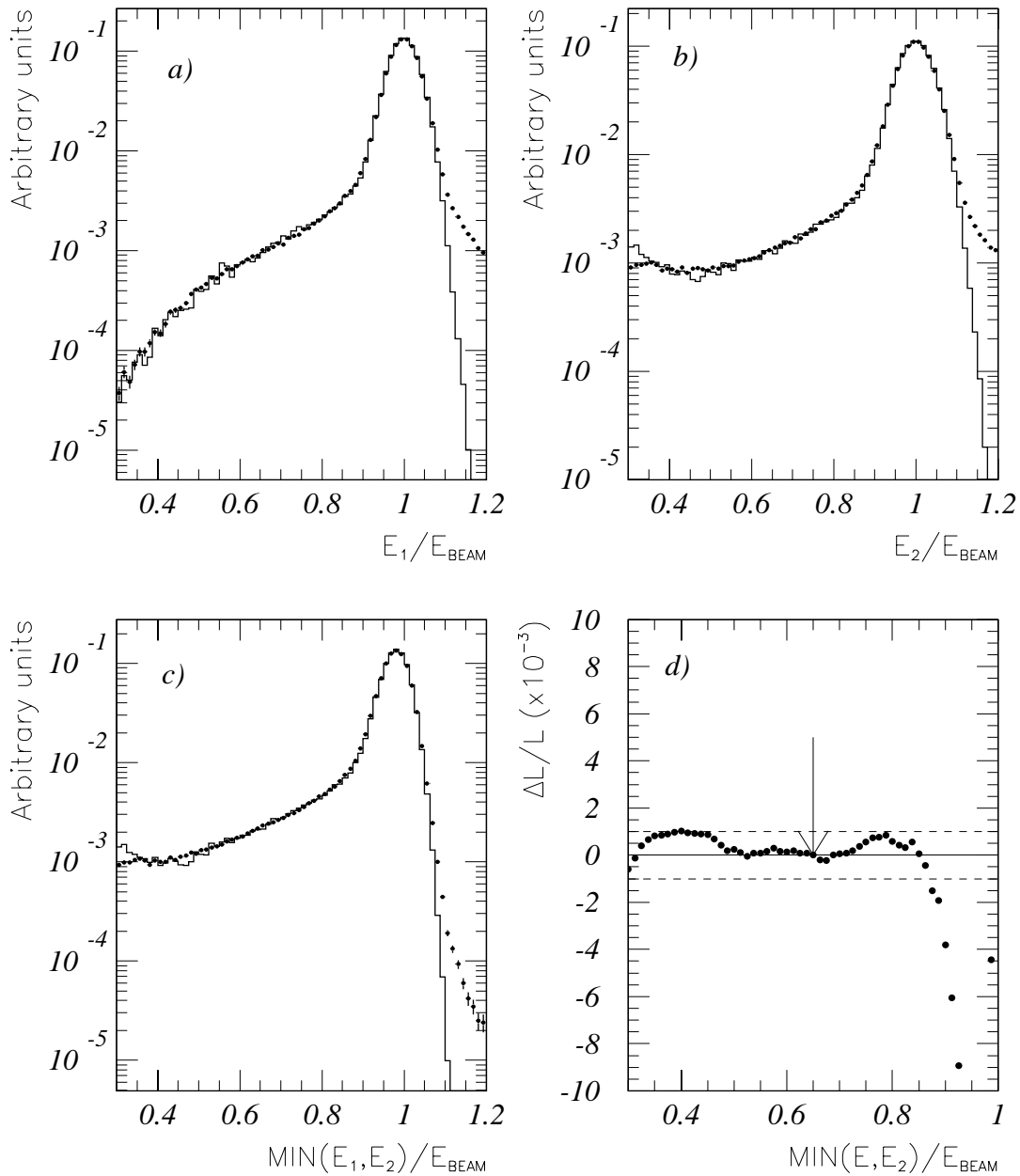


Figure 1: (a), (b) The relative energy distributions for the 1993 data in the two SAT calorimeters separately and (c) the relative minimum energy distribution for data (points) and simulated data (histograms) after all other event selection criteria have been applied. (d) The variation of the measured luminosity with respect to the placement of the minimum energy cut. The luminosity change is defined to be zero at the standard cut of 65% of the beam energy, indicated by the arrow.

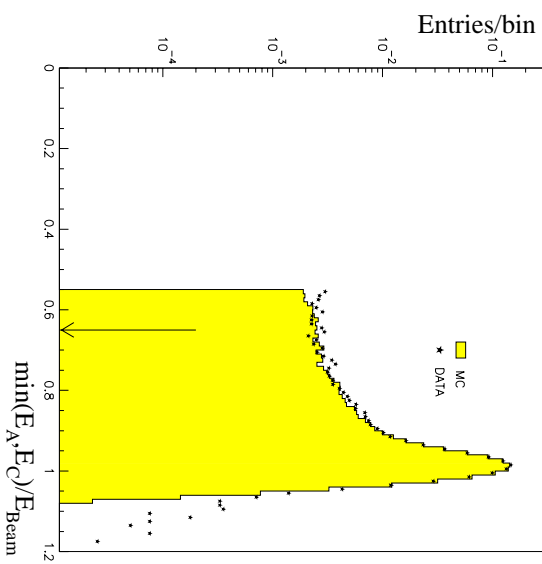


Figure 2: Distribution for 1994 data of E_A or E_C , the energies of the highest energy clusters in each of the STIC arms. The smaller of E_A or E_C has been plotted. The arrow shows the position of the cut used in selecting Bhabha events.

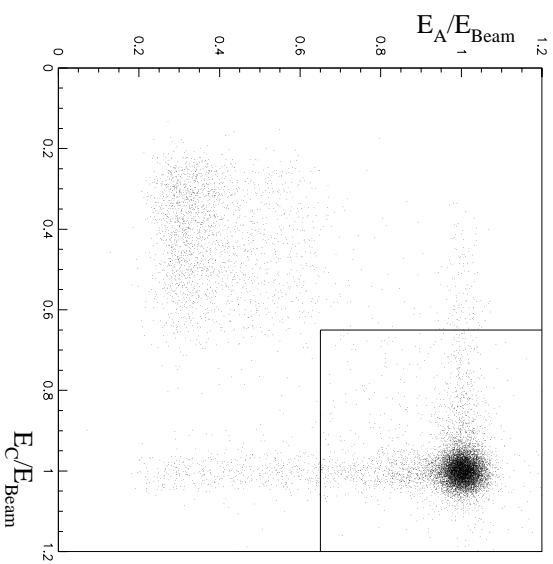


Figure 3: Distribution for 1994 data of the highest energy cluster of one STIC arm versus the highest energy cluster of the other: the selected region is indicated by the box.

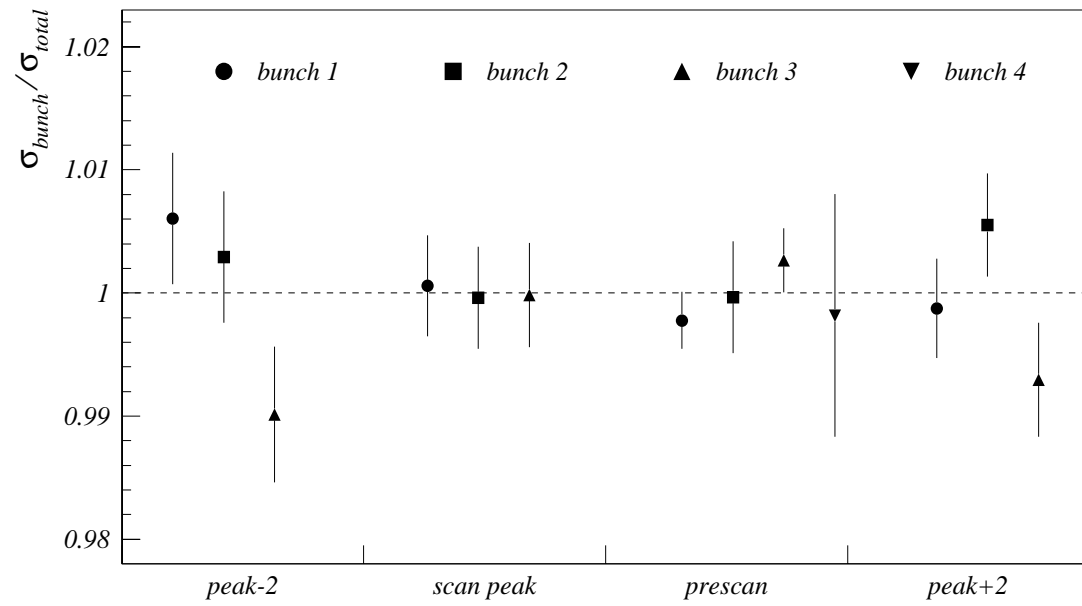


Figure 4: Hadronic cross-section per bunch divided by the total hadronic cross-section at each collision energy in 1995. A fourth bunch was used only during the “prescan” period.

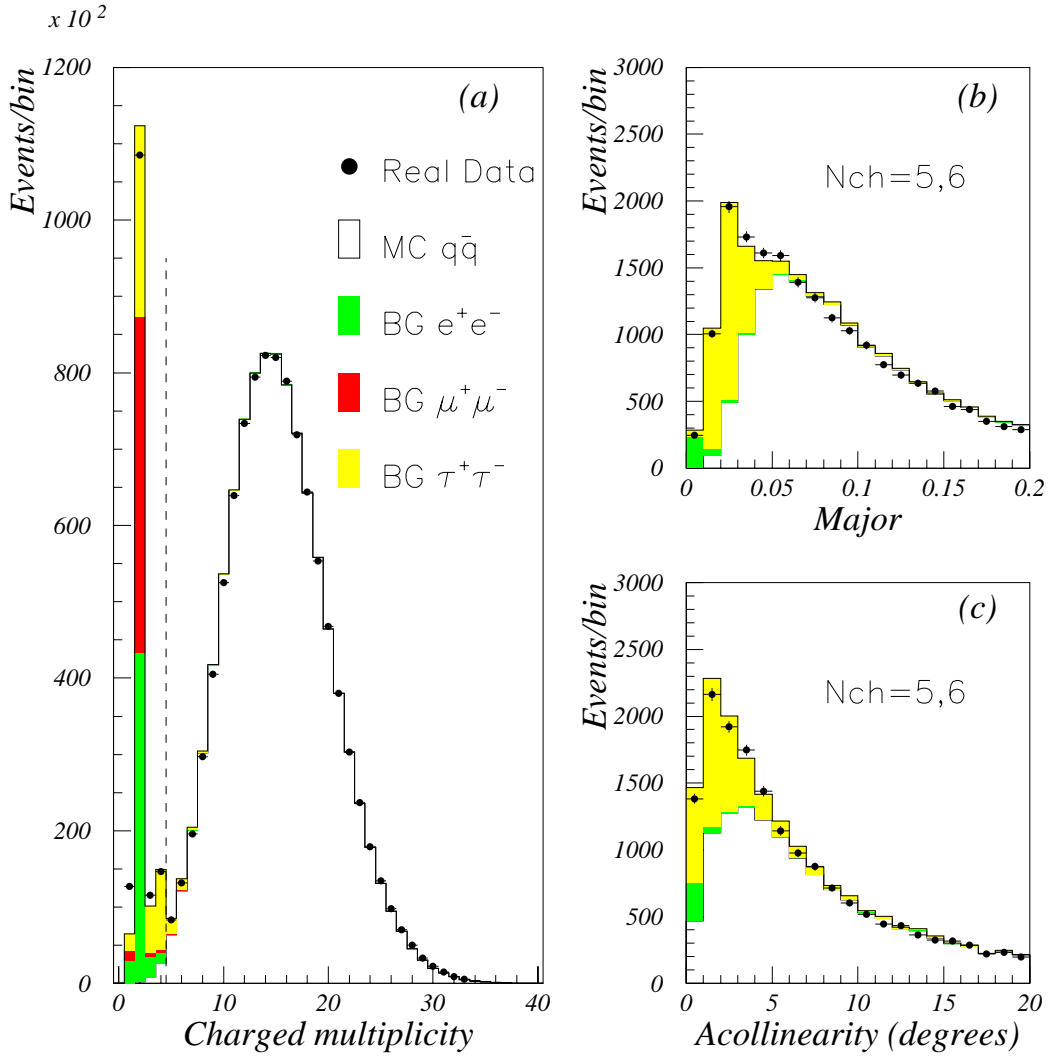


Figure 5: Distribution of (a) the charged multiplicity, (b) the major value of the transverse momentum with respect to the event thrust axis and (c) the acollinearity between the momenta of both event hemispheres, for hadronic events at the peak energy. The multiplicity distribution is shown for events satisfying all other selection criteria with the dashed vertical line showing the charged multiplicity cut. The acollinearity and the major distributions are restricted to selected events with charged multiplicity 5 and 6. Points with error bars represent the data. The white areas show the predictions of the JETSET model. The shaded areas show the contributions from the main background processes visible on these distributions: $\tau^+\tau^-$ pairs (light grey), e^+e^- pairs (medium grey) and $\mu^+\mu^-$ pairs (dark grey).

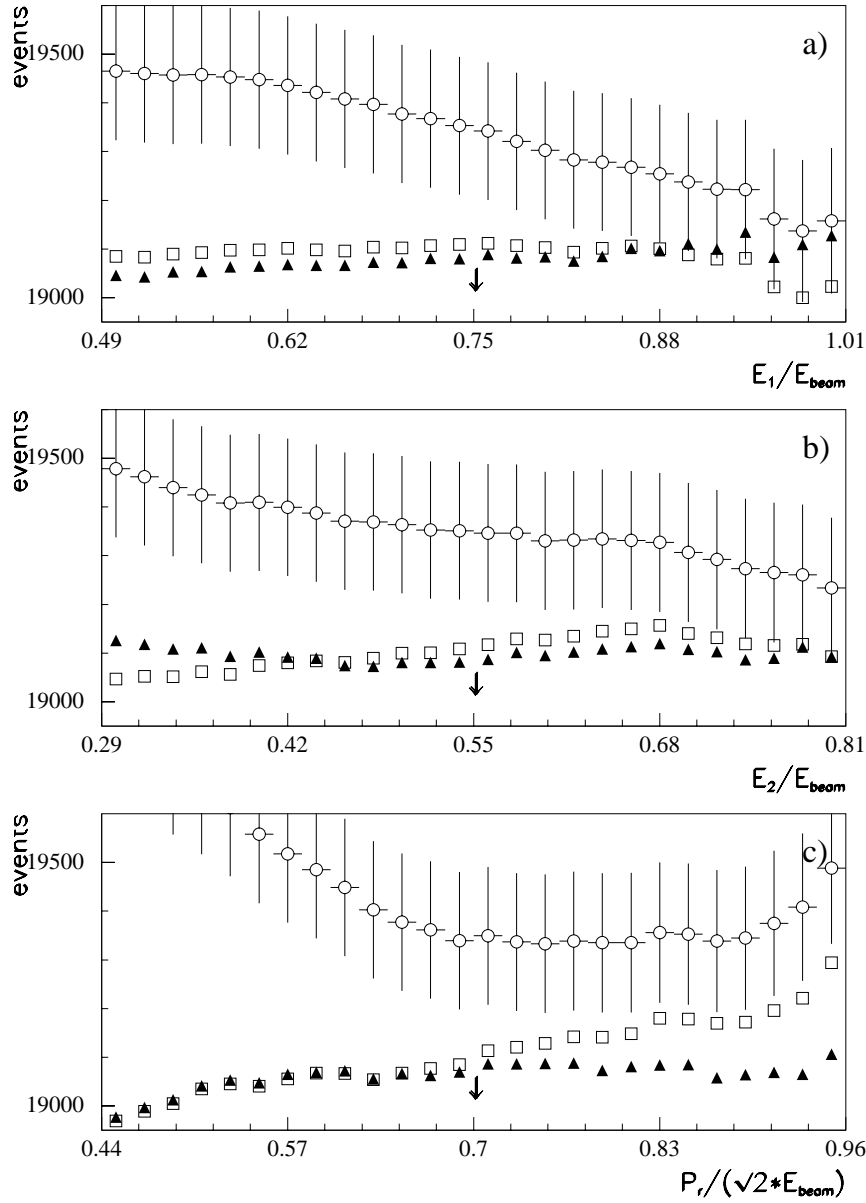


Figure 6: Total number of e^+e^- events estimated by method 2 at the scan energies, as a function of some of the cut variables: a) energy of the most energetic electromagnetic cluster, normalized to the beam energy, b) energy of the second most energetic electromagnetic cluster, normalized to the beam energy, c) quadratic sum of the momenta of the two highest momentum charged particles, normalized to $\sqrt{2}$ times the beam energy. The circles give the estimated number of events after efficiency correction (the statistical uncertainty is shown - the numbers of events and the statistical uncertainties are correlated between successive values of the cut variables), the squares after background subtraction and the triangles after correlation correction. The chosen cut value is indicated with an arrow.

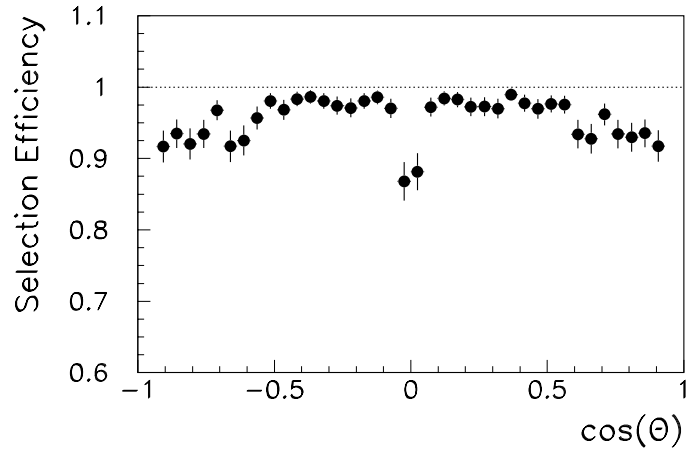


Figure 7: The total selection efficiency in 1994 for events $e^+e^- \rightarrow \mu^+\mu^-$ versus the cosine of the polar angle for the faster muon.

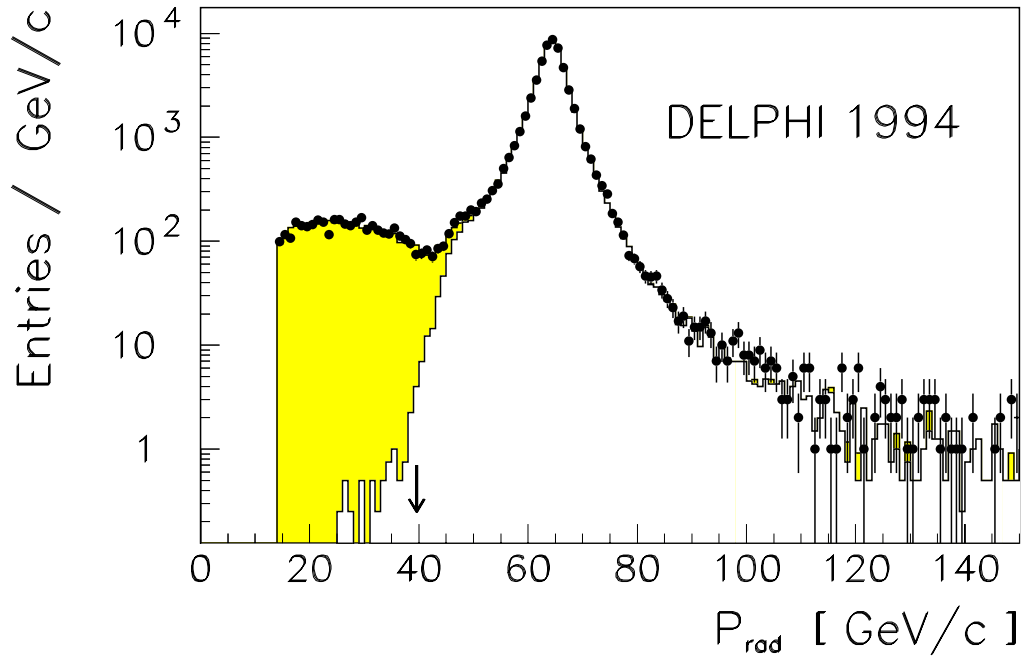


Figure 8: Distribution of the event variable P_{rad} for data from the 1994 running period (points) and the fitted Monte Carlo. The unshaded area is the contribution from $\mu^+\mu^-$, and the shaded area is the contribution from $\tau^+\tau^-$. The arrow indicates the cut applied in the final event selection.

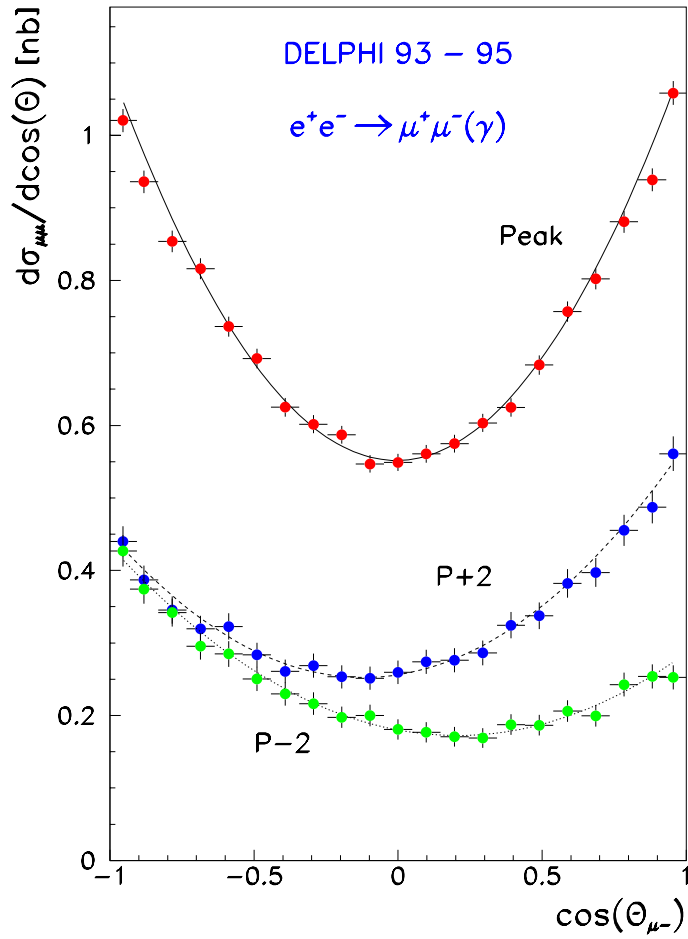


Figure 9: Differential cross-sections of the reaction $e^+e^- \rightarrow \mu^+\mu^-$ combined for the years 1993 to 1995. The curves are fits to the data points assuming the lowest order form of the differential cross-section.

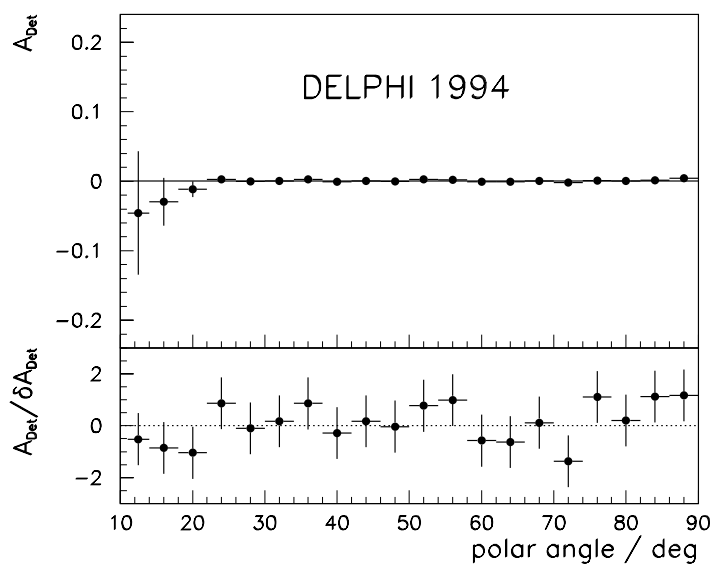


Figure 10: Muon detection asymmetry A_{det} versus the polar angle as determined for the 1994 running period, both as an absolute quantity, and normalized by its statistical uncertainty, δA_{det} .

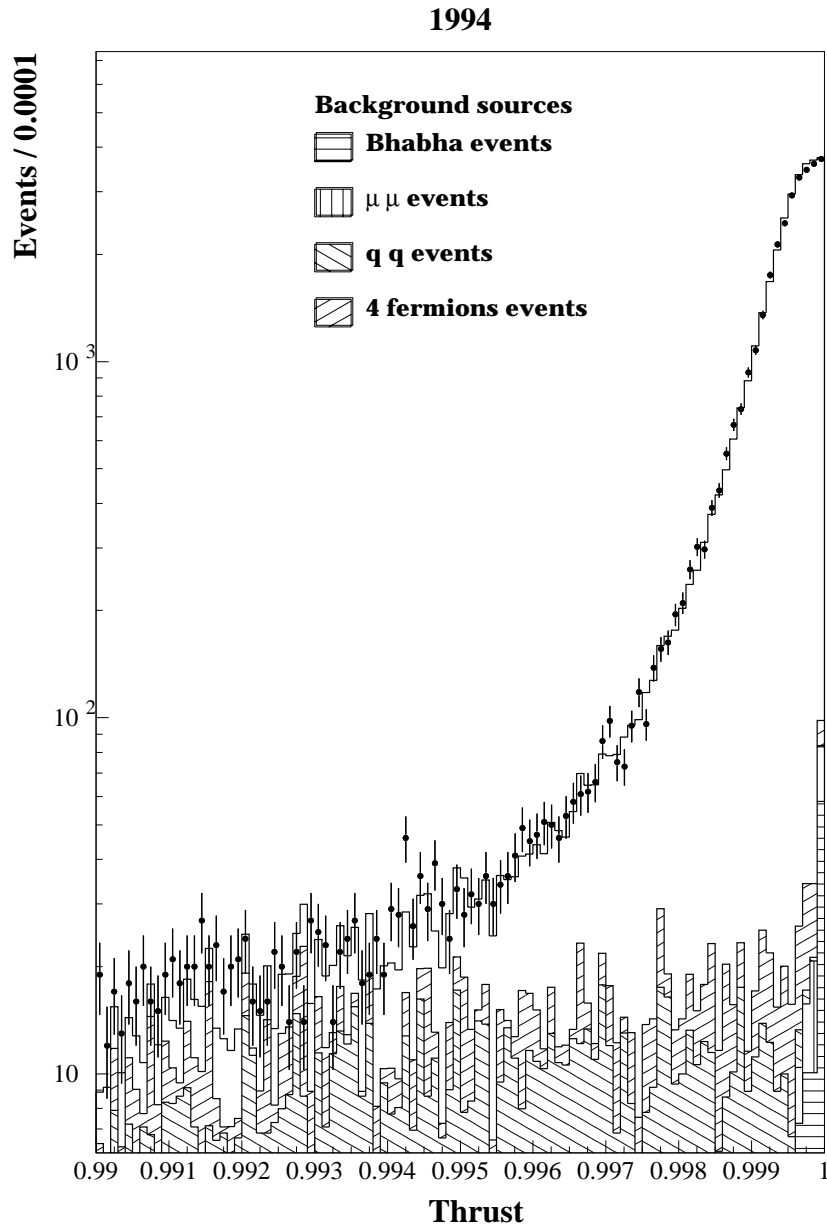


Figure 11: The distribution of the thrust variable for events selected as $\tau^+\tau^-$ in 1994. The points are for the data, the open area is for simulated $\tau^+\tau^-$ events and the cross-hatched areas represent the simulated background from all sources. Only events with Thrust > 0.996 are retained. The plot shows that the data are well reproduced by the simulation.

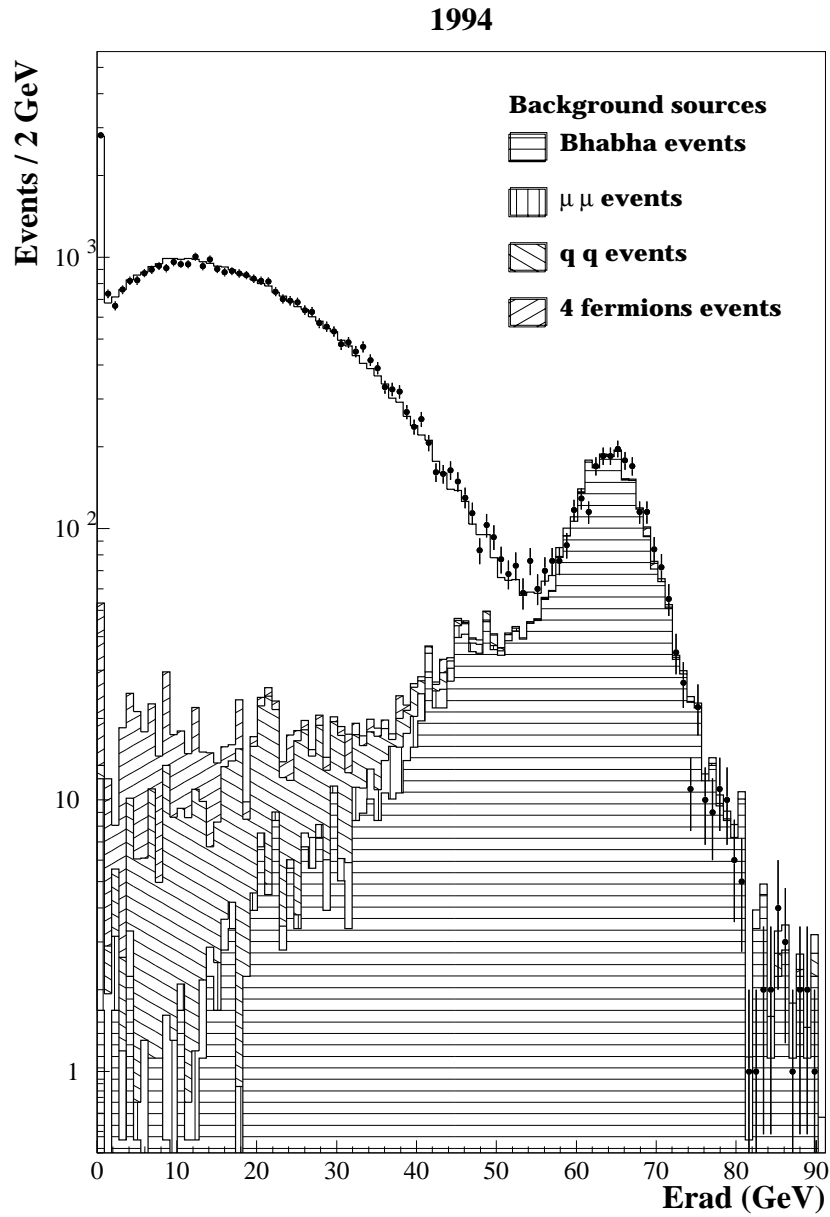


Figure 12: The distribution of the E_{rad} variable in events selected as $\tau^+\tau^-$ candidates in 1994. The points are for the data, the open area is for simulated $\tau^+\tau^-$ events and the hatched areas represent the simulated backgrounds. Only events with $E_{rad} < \sqrt{s}/2$ are retained. The plot shows that the data are well reproduced by the simulation.

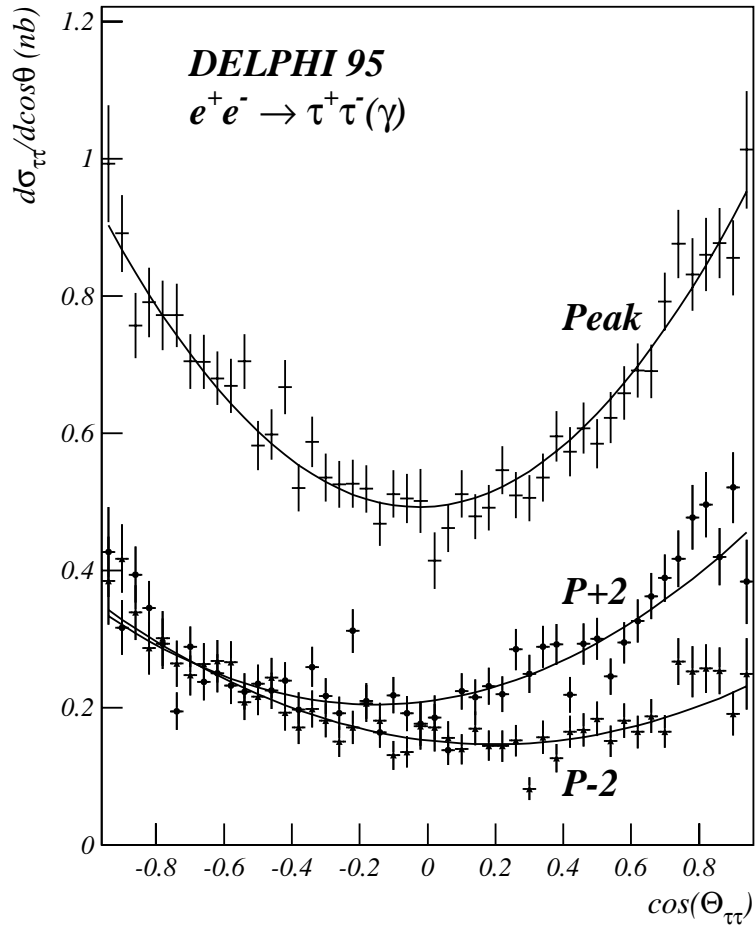


Figure 13: Differential cross-sections in the $\tau^+\tau^-$ channel as measured at the three energy values in 1995. The curves are fits to the lowest order form of the angular distribution.

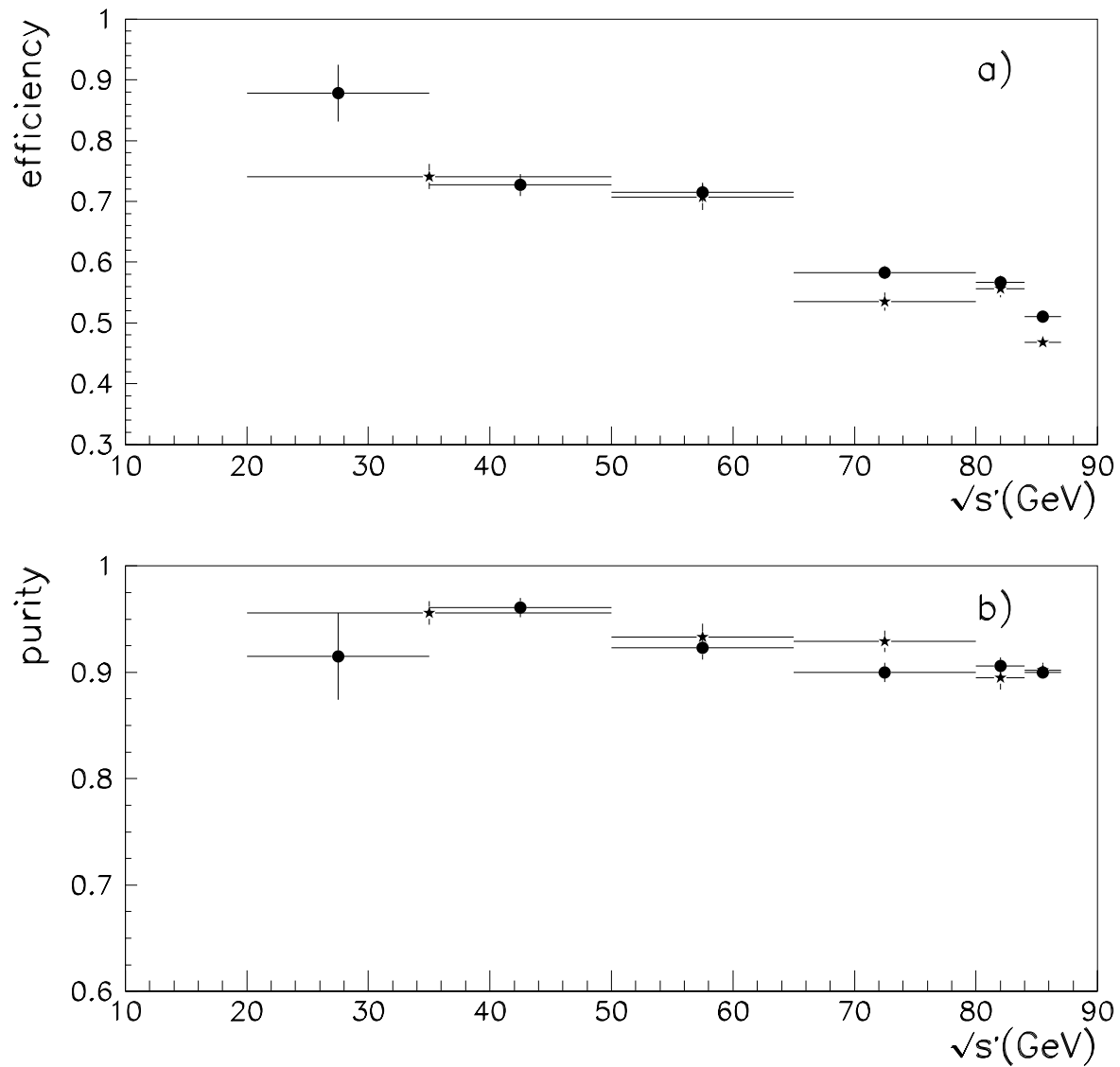


Figure 14: (a) Efficiency for the selection of ISR events and (b) purity of the ISR sample with regard to FSR events, based on simulated radiative muon events, for the 1991-1994 data [27] (black dots) and for the data taken in 1995 (stars).

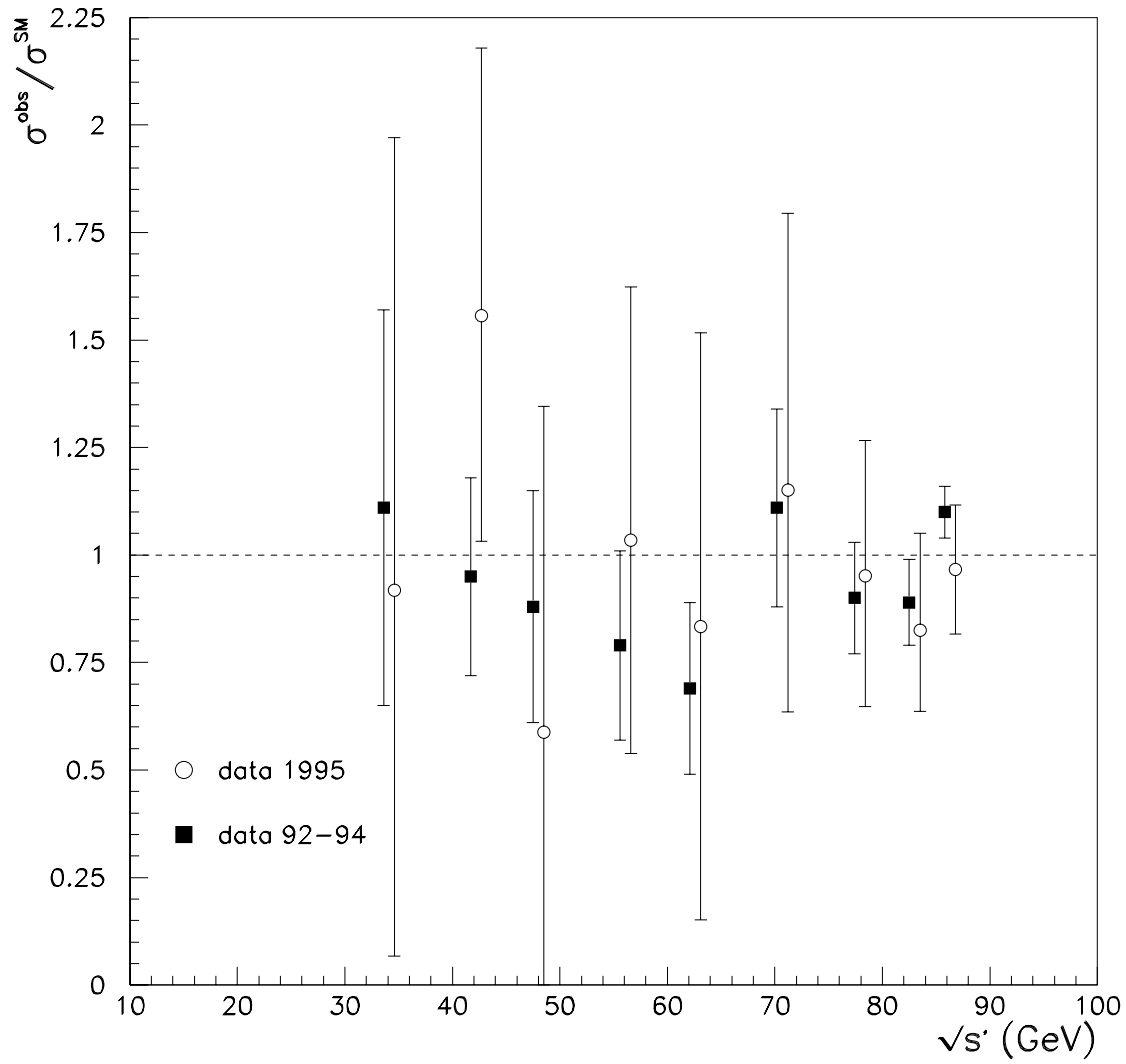


Figure 15: Ratio of measured to SM Improved Born $\mu^+\mu^-$ cross-sections as a function of the effective annihilation energy.

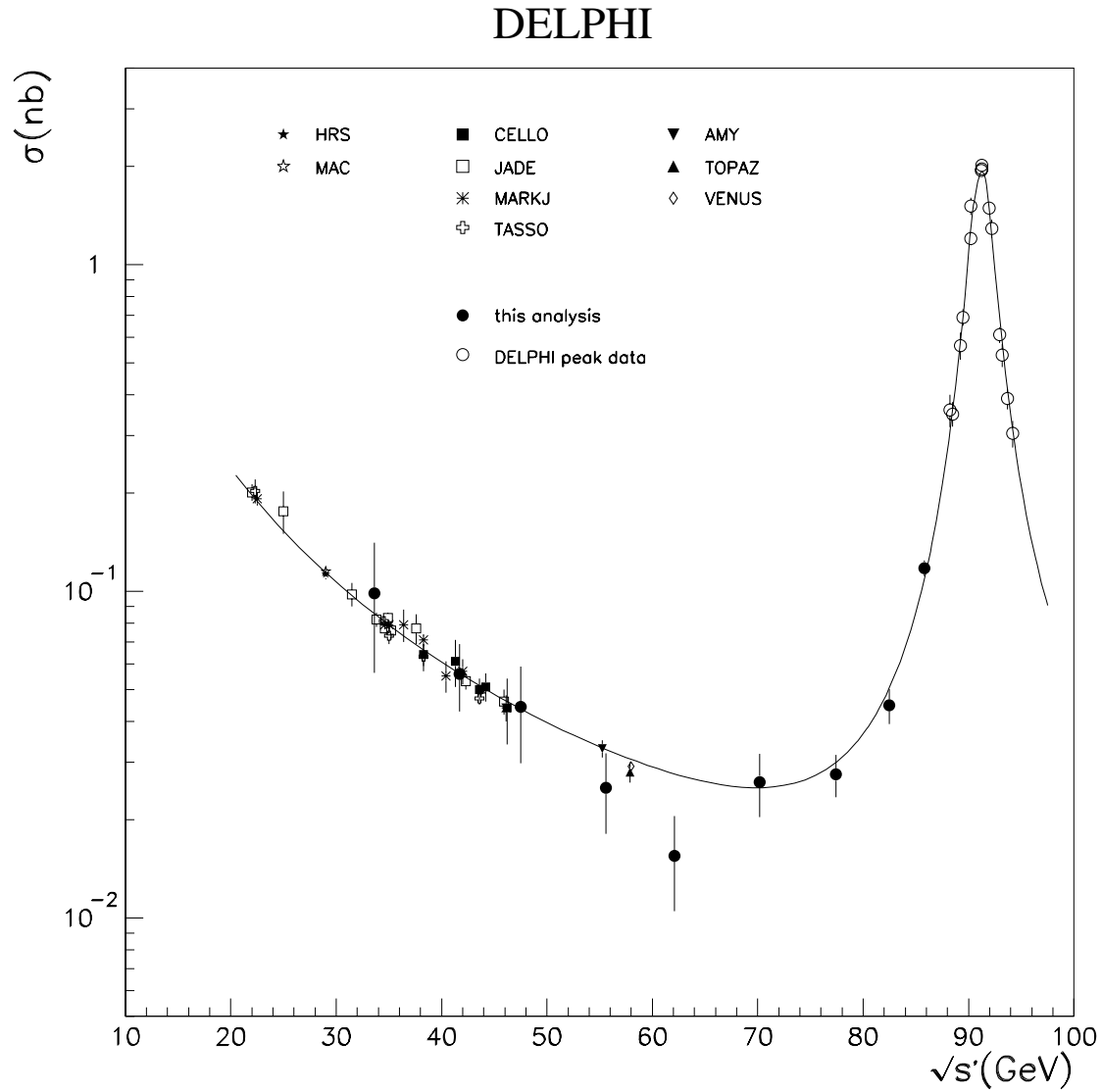


Figure 16: Cross-sections in the Improved Born Approximation for $\mu^+\mu^-$ as measured in the analysis of DELPHI data from 1992 to 1995 (*black circles*), at the Z^0 peak (*open circles*), and at PEP, PETRA and TRISTAN. The curve shows the SM prediction.

DELPHI

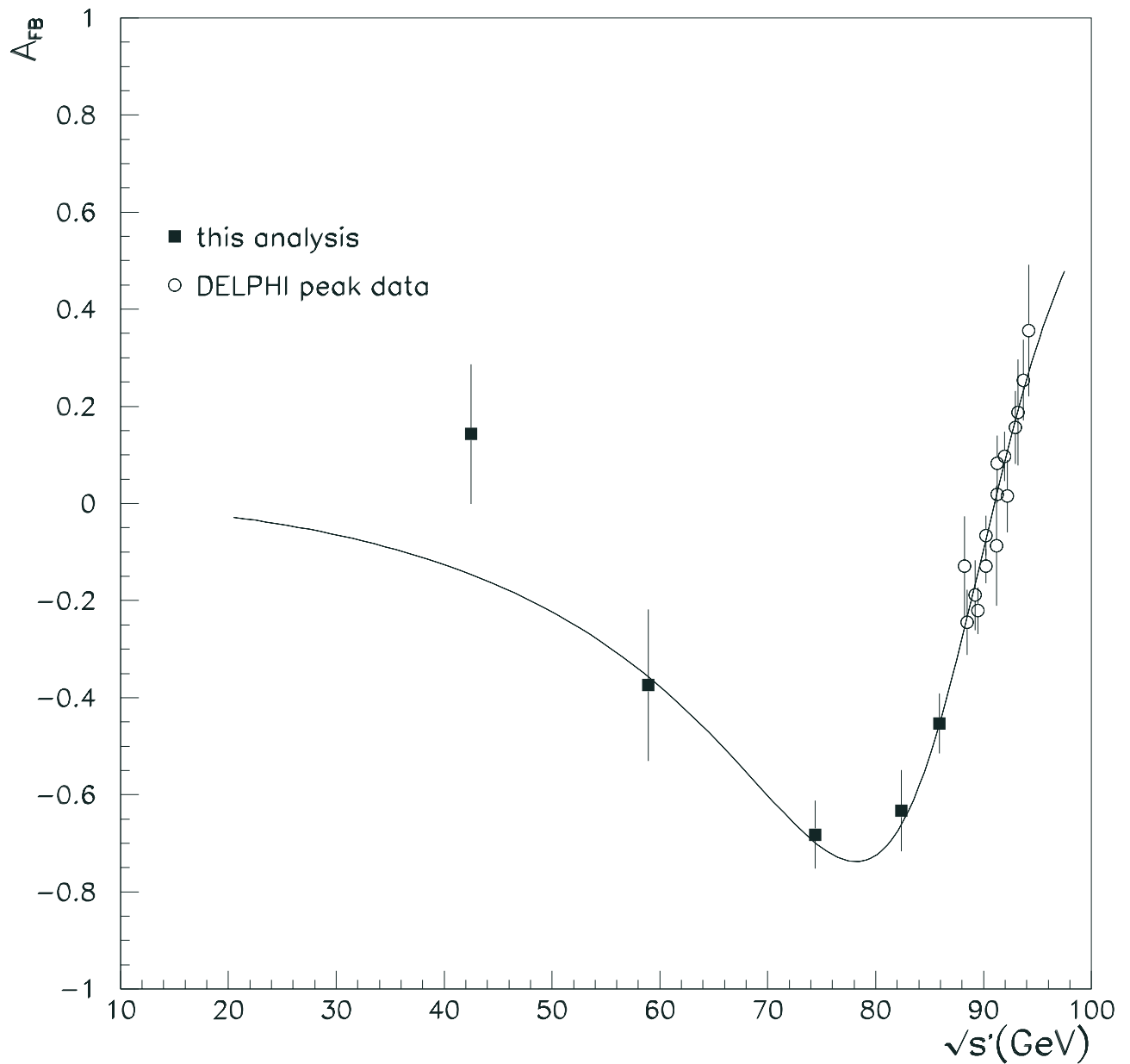


Figure 17: Improved Born $\mu^+\mu^-$ asymmetry as a function of the effective annihilation energy. The *black squares* show the measurements made by DELPHI below $\sqrt{s} = 87$ GeV, using the likelihood fit method described in the text. The *open circles* show the measurements made by DELPHI at the Z^0 peak. The curve shows the SM prediction.

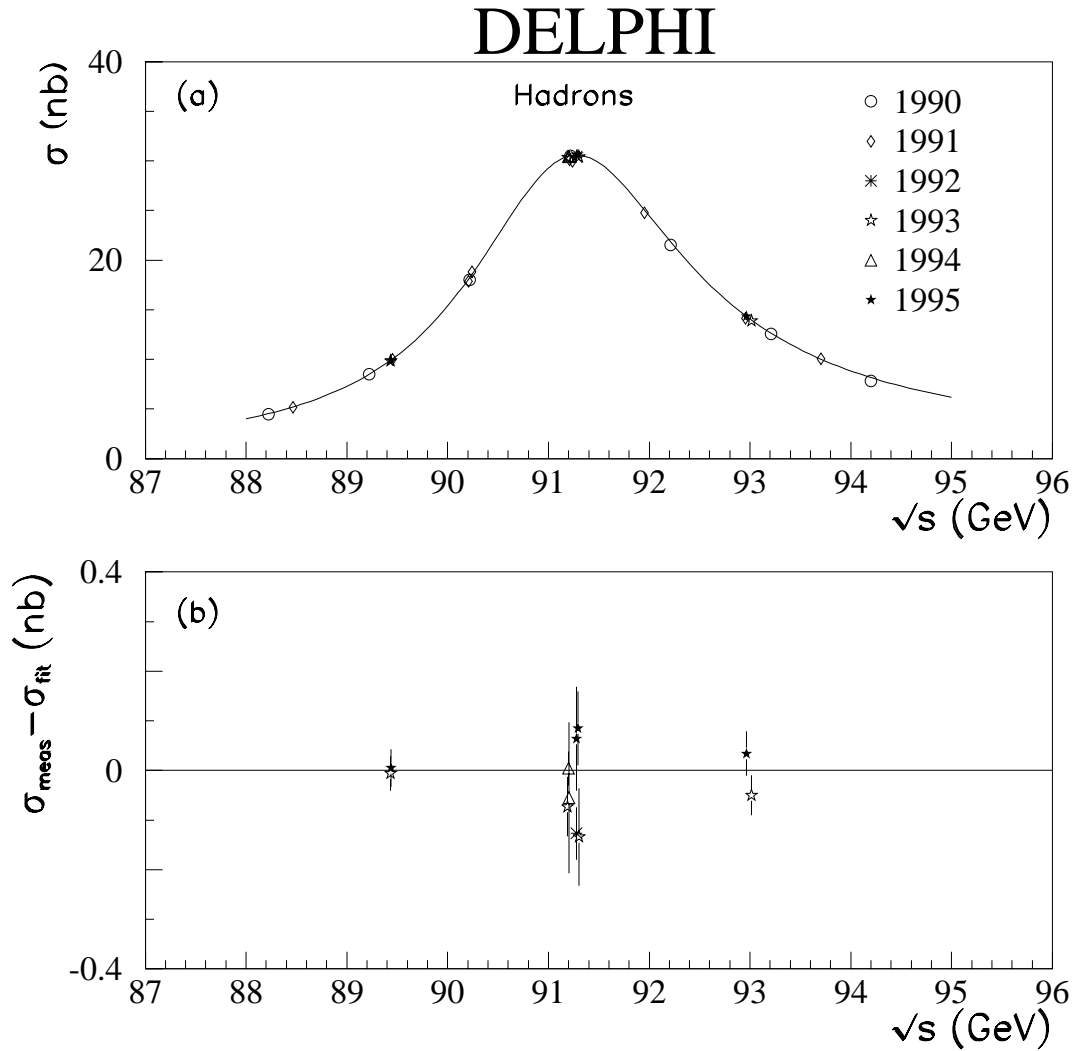


Figure 18: Hadronic cross-sections from 1990, 1991, 1992, 1993, 1994 and 1995 data. The uncertainties shown are statistical only. In (a) the data are shown together with a curve representing the result of the 5-parameter fit described in Section 10. Plot (b) shows the difference of the measurements from the best fit values; for clarity only the data from 1992, 1993, 1994 and 1995 are shown.

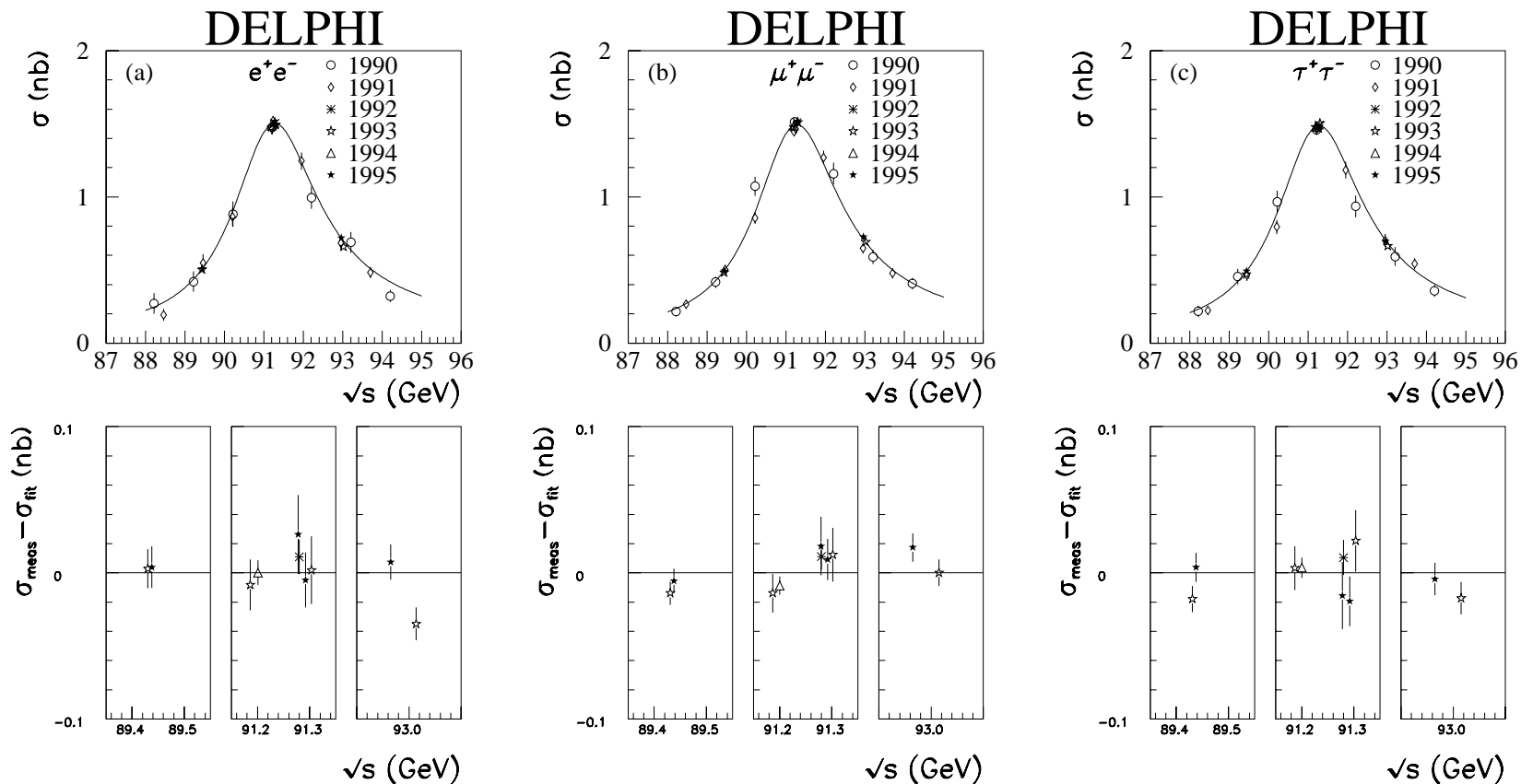


Figure 19: Cross-sections in the (a) e^+e^- , (b) $\mu^+\mu^-$ and (c) $\tau^+\tau^-$ channels; for e^+e^- the t-channel contribution has been subtracted. The cross-sections are corrected for the acollinearity and momentum cuts and extrapolated to the full solid angle. Only statistical uncertainties are shown. The lower plots show the differences between the measured points and the best fit values; for clarity only the 1992, 1993, 1994 and 1995 data are shown. The curves represent the results of the 5-parameter fit described in Section 10.

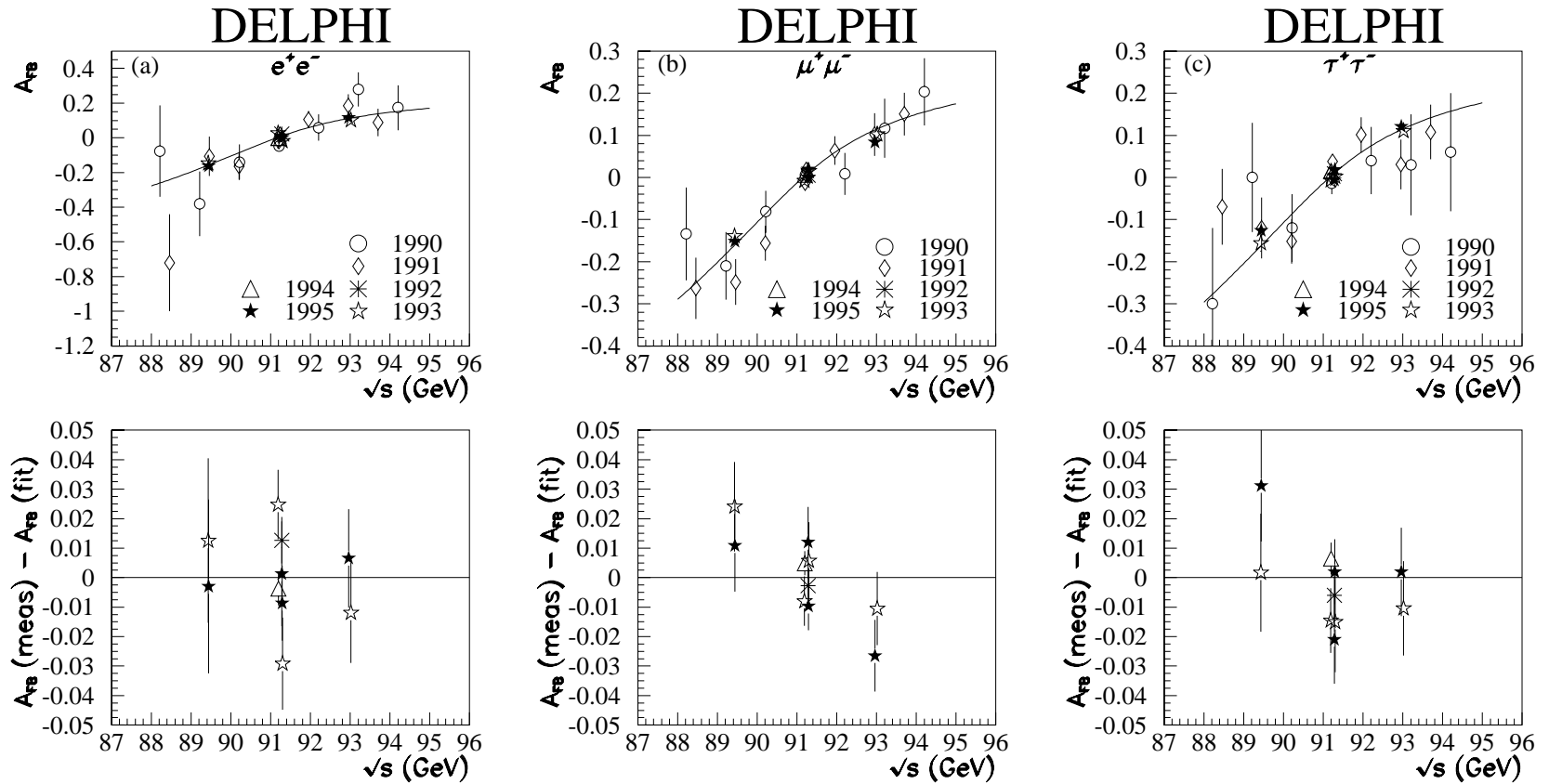


Figure 20: Forward-backward asymmetries in the (a) e^+e^- , (b) $\mu^+\mu^-$ and (c) $\tau^+\tau^-$ channels. The asymmetries are corrected for the acollinearity and momentum cuts and extrapolated to the full solid angle. The lower plots show the differences between the measured points and the best fit values; for clarity only the 1992, 1993, 1994 and 1995 data are shown. The curves represent the results of the 5-parameter fit described in Section 10.